

JGR Space Physics

RESEARCH ARTICLE

10.1029/2020JA028846

Key Points:

- An explicit algorithm for the quadratic magnetic gradient based on multipoint measurements with iterations is presented for the first time
- The algorithm is applicable for both steady and unsteady structures, and the obtained linear magnetic gradient has second order accuracy
- The complete geometry of the magnetic field lines has been obtained, for the first time, based on multipoint measurements

Supporting Information:

Supporting Information may be found in the online version of this article.

Correspondence to:

C. Shen,
shenchao@hit.edu.cn

Citation:



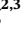








Shen, C., Zhang, C., Rong, Z., Pu, Z., Dunlop, M. W., Escoubet, C. P., et al. (2021). Nonlinear magnetic gradients and complete magnetic geometry from multispacecraft measurements. *Journal of Geophysical Research: Space Physics*, 126, e2020JA028846. <https://doi.org/10.1029/2020JA028846>

Received 1 NOV 2020
 Accepted 28 JUN 2021

© 2021. The Authors.

This is an open access article under the terms of the [Creative Commons Attribution License](https://creativecommons.org/licenses/by/4.0/), which permits use, distribution and reproduction in any medium, provided the original work is properly cited.

Nonlinear Magnetic Gradients and Complete Magnetic Geometry From Multispacecraft Measurements

Chao Shen¹ , Chi Zhang^{2,3} , Zhaojin Rong^{2,3} , Zuyin Pu⁴ , Malcolm W. Dunlop^{5,6} , C. Philippe Escoubet⁷ , C. T. Russell⁸ , Gang Zeng⁹ , Nian Ren¹ , James L. Burch¹⁰ , and Yufei Zhou¹ 

¹School of Science, Harbin Institute of Technology, Shenzhen, China, ²Institute of Geology and Geophysics, Chinese Academy of Sciences, Beijing, China, ³College of Earth Science, University of Chinese Academy of Sciences, Beijing, China, ⁴School of Earth and Space Sciences, Peking University, Beijing, China, ⁵School of Space and Environment, Beihang University, Beijing, China, ⁶Rutherford Appleton Laboratory, Chilton, Didcot, UK, ⁷ESA/ESTEC (SCI-SC), Noordwijk, The Netherlands, ⁸University of California, Los Angeles, CA, USA, ⁹School of Mathematics and Physics, Jingchu University of Technology, Jingmen, China, ¹⁰Southwest Research Institute, San Antonio, TX, USA

Abstract Topological configurations of the magnetic field play key roles in the dynamics of space plasmas. This study presents a novel algorithm that can estimate the quadratic magnetic gradient as well as the complete geometrical features of magnetic field lines, based on magnetic field and current density measurements by a multiple spacecraft constellation at four or more points. The explicit estimators for the linear and quadratic gradients, the apparent velocity of the magnetic structure and the curvature and torsion of the magnetic field lines can be obtained with well-predicted accuracies. The feasibility and accuracy of the method have been verified with two demonstrations. The algorithm has been successfully applied to exhibit the geometrical structure of a flux rope. This algorithm has wide applications for studying a variety of magnetic configurations in space plasmas.

Plain Language Summary The magnetic field plays a key role in the dynamical evolution of space plasmas; it traps and stores plasma particles, and controls the transfer, conversion, and release of the energies. The magnetic field can form various structures, where the magnetic field lines can bend and twist. At the present time, full imaging of the magnetic field has not been achieved. Therefore, it is very important to estimate the magnetic gradients at every order, as well as the geometrical features (curvature and torsion) of the magnetic field lines (MFLs), from the in situ observations. Although we have successfully deduced the first order magnetic gradient and the curvature from multiple S/C magnetic measurements, how to estimate the high order magnetic gradients and the torsion of MFLs is still unsolved. Here, for the first time, we put forward a novel explicit algorithm, which can acquire the quadratic magnetic gradient and the torsion of MFLs with the four-point magnetic field and current density measurements as the input. This algorithm has sound accuracies and can be effectively applied to analyze magnetospheric multiscale (MMS) observations. This method has many applications in space exploration and theoretical and applied research.

1. Introduction

A magnetic field can trap plasma populations; control the transfer, conversion, and release of energy in planetary magnetospheres; play a key role in the spatial distribution of the plasmas and development of instabilities, as well as control the evolution of substorms and storms. The measurement of the magnetic field in space has recently been carried out using a limited number of sometime collocated spacecraft in various locations. It is both important and possible to establish the continuous distribution of the magnetic field, based on these multipoint magnetic observations. With two-point measurements, the gradient of the magnetic field along the spacecraft (S/C) separation line can be obtained; With three-point magnetic measurements, the magnetic gradient within the S/C constellation plane can be determined; while with four or more distributed magnetic measurements, the three dimensional (3-D) linear magnetic gradient (also called as the first order gradient or Jacobian matrix) can be estimated (Chanteur, 1998; Dunlop et al., 2015, 2016, 2018, 2020; Harvey, 1998; McComas et al., 1986; Shen, Rong, Dunlop et al., 2012; Shen,

Rong, & Dunlop, 2012; Vogt et al., 2008). In order to get the quadratic magnetic gradient (also called as the second order gradient or Hessian tensor), 10 S/C magnetic measurements are needed (Chanteur, 1998).

In the past, magnetic measurements have been performed with two S/C (ISEE-1/2, DSP, RBSP, ARTEMIS, etc.) (Angelopoulos, 2008; Z.-X. Liu et al., 2005; Ogilvie et al., 1977; Shen & Liu, 2005), three S/C constellations (THEMIS, Swarm) (Angelopoulos, 2008; Friis-Christensen et al., 2006), and four S/C constellations (Cluster and magnetospheric multiscale [MMS]) (Balogh et al., 2001; Burch et al., 2016; Escoubet et al., 2001; Russell et al., 2016). However, presently 10 S/C magnetic field observations in space are still on the drawing boards. Deducing the various orders of magnetic gradients fully with a limited number of S/C observations remains an important unsolved problem.

Attempts to partially solve this problem have used physical constraints to assist the complete determination of the magnetic gradients (Vogt et al., 2009). The symmetries in plasma structures and the electromagnetic field laws can also be useful. It has been found by Shen, Rong, Dunlop et al. (2012) that, for a force-free magnetic structure in which the current is field-aligned, the 3-D magnetic gradient can be completely obtained with 3 spacecraft magnetic measurements. In their derivation, Ampere's law $\nabla \times \mathbf{B} = \mu_0 \mathbf{j}$ and the solenoidal condition of the magnetic field $\nabla \cdot \mathbf{B} = 0$ are used to reduce the equations. Furthermore, if the force-free magnetic structure is steady and moving with a known relative velocity, only two S/C magnetic observations are needed to gain the complete nine components of the linear magnetic gradient (Shen, Rong, & Dunlop, 2012). Y. Y. Liu et al. (2019) have suggested a method to get the nonlinear distribution of the magnetic field in a stationary plasma structure by fitting the second-order Taylor expansion based on 4 S/C magnetic measurements and one S/C current density observation, where Ampere's law and the solenoidal condition of the magnetic field was also used. Torbert et al. (2020) have successfully obtained the 3D distribution of the magnetic field by using the four-point magnetic and particle/current density measurements of MMS. In their exploration, they have applied a fitting method to the magnetic field to the third order in magnetic gradient $((\partial_m \partial_l \partial_k B_j)_0)$, called the "25-parameter fit." In addition, the second order derivative of the magnetic field at the minimum variation direction in the local MVA characteristic coordinates was regarded as zero. Denton et al. (2020) have reconstructed the magnetic structures with a fitting method in the local characteristic coordinates system (Shi et al., 2005) and explored the contributions of various linear and quadratic terms in detail. However, there still exists no explicit solution to the determination of the quadratic magnetic gradient based on multiple spacecraft measurements.

With multiple S/C magnetic observations, geometrical features of the magnetic field lines can be obtained (Rong et al., 2011; Shen et al., 2003, 2011, 2014; Shen, Liu, et al., 2008; Shen, Rong, et al., 2008; Lavraud et al., 2016; Xiao et al., 2018). The geometry of the magnetic field lines (MFLs) so obtained includes the tangential direction (just the direction of the magnetic vector), principal direction (along the curvature vector), binormal vector (the normal of the osculating plane of one MFL), curvature, and torsion. However, the torsion of the MFLs has not been obtained in these previous methods. The reason for this is that the torsion of the MFLs depends on the quadratic magnetic gradient, which needs 10-point S/C magnetic measurements (Chanteur, 1998) to be deduced. Therefore, it is necessary to explore the calculation of the torsion of MFLs based on observations of a limited number of S/C, in order to gain this more complete picture of MFLs in space.

This problem is addressed herein, where an explicit algorithm has been derived to estimate the quadratic magnetic gradient as well as the complete geometrical parameters of the MFLs based on measurements with a limited number of spacecraft. This approach has a wide range of applications for analyzing the magnetic structure in space plasmas.

In Section 2 and Appendices A and B, the algorithm for the quadratic magnetic gradient is derived. In Section 3 and Appendix C, the general differential geometric properties of magnetic field lines are addressed. In Sections 4, the new approach has been demonstrated on the Harris current sheets and cylindrical flux ropes in comparison with the analytical features of these two kinds of magnetic structures illustrated in Appendices D and E. Section 5 presents an actual application of this algorithm for analyzing the magnetic structure of one flux rope observed by MMS. Section 6 gives the summary and discussions.

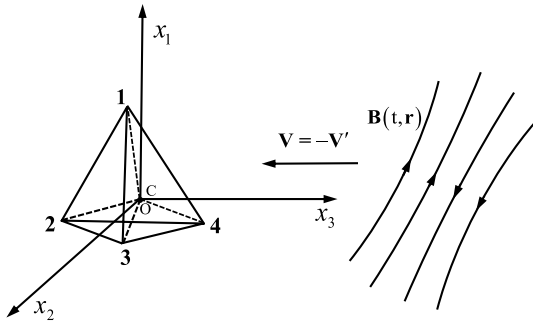


Figure 1. The exploration of the magnetic field in space in the S/C constellation frame of reference. (x_1, x_2, x_3) are the Cartesian coordinates in the S/C constellation reference frame. The S/C constellation is composed of four spacecraft (the number of spacecraft can be more 4), whose barycenter is at the point C. C has been set as the origin of the coordinates in the constellation reference frame. The apparent motional velocity of the magnetic field structure relative to the S/C constellation reference is V . Conversely, the velocity of the S/C constellation relative to the proper reference of the magnetic field structure is $V' = -V$.

2. The Estimators for the Linear and Quadratic Gradients of Magnetic Field

It is very important to obtain the quadratic gradient of the magnetic field. With it, we can grasp more accurately the structure of the magnetic field and, uncover the complete geometrical structure of the MFLs, including the Frenet coordinates and curvature, as well as the torsion. In this section, we obtain the explicit estimator of the quadratic magnetic gradient based on magnetic field and current density measurements from a multi-S/C constellation.

We present the derivation of this algorithm as follows.

The configuration of the four-spacecraft constellation (Cluster or MMS) is illustrated in Figure 1.

In the S/C constellation frame of reference, the simultaneous position vectors of the four spacecraft are r_α ($\alpha = 1, 2, 3, 4$) and the position vector of the barycenter of the four S/C is

$$r_c = \frac{1}{4} \sum_{\alpha=1}^4 r_\alpha. \quad (1)$$

In this study, the Greek subscripts or superscripts apply to spacecraft and $\alpha, \beta, \gamma, \dots = 1, 2, 3, 4$; while the Latin subscript c indicates the barycenter.

The apparent motional velocity of the magnetic field structure relative to the S/C constellation reference frame is denoted as V , which may vary from point to point (Hamrin, et al., 2008). The velocity of the S/C constellation relative to the proper reference frame of the magnetic field structure is $V' = -V$. We establish the Cartesian coordinates (x_1, x_2, x_3) in the S/C constellation reference, and choose the x_3 axis along the direction of $V' = -V$ with its basis $\hat{x}_3 = -V / V$. The configuration of the S/C constellation is characterized by the volume tensor, which is defined (Harvey, 1998; Shen et al., 2003) as

$$R_{kj} = \frac{1}{4} \sum_{\alpha=1}^4 (r_{\alpha k} - r_{c k})(r_{\alpha j} - r_{c j}). \quad (2)$$

Here, and in the text below, we apply some Latin subscripts or superscripts (other than c) to denote Cartesian coordinates with $i, j, k, e, m, n = 1, 2, 3$ and $p, q, s, r = 1, 2$.

(i) The linear gradients of the magnetic field and current density at the barycenter

As the MMS S/C cross a magnetic structure, the four S/C measure the magnetic field with high accuracy and time resolution (Burch et al., 2016; Russell et al., 2016). The magnetic field observed by the α th S/C at position r_α is

$$B_\alpha(t) = B(t, r_\alpha), \alpha = 1, 2, 3, 4. \quad (3)$$

The MMS S/C can measure the distributions of ions and electrons with sufficient accuracy to yield the local current density (Pollock et al., 2016; Torbert et al., 2015, 2020) as

$$j_\alpha(t) = j(t, r_\alpha), \alpha = 1, 2, 3, 4. \quad (4)$$

To obtain the magnetic field and its first order gradient at the barycenter of the MMS constellation, we first neglect the second order magnetic gradient under the linear approximation. With four S/C, simultaneous magnetic observations, the magnetic field and its linear gradient at the barycenter of the S/C constellation can be obtained with the previous methods established by Harvey (1998) and Chanteur (1998). In order to suppress the fluctuating components in the magnetic field and obtain the magnetic gradient at higher accuracy, we make use of the time series of the magnetic observations by the four S/C to get the magnetic gradient with the method first put forward by De Keyser, et al. (2007). In their approach, the time series

data of the four S/C do not need to be synchronized. Appendix A gives the explicit estimator of the linear gradient of magnetic field in space and time with corrections from the quadratic gradients.

Based on Equations A14 and A15 in Appendix A, the magnetic field and its first order derivatives at the barycenter of the MMS constellation under the linear approximation are as follows.

$$B_i(t_c, r_c) = \frac{1}{4n} \sum_{a=1}^{4n} B_i(t_a, r_a), \quad (5)$$

$$\nabla_v B_i(t_c, r_c) = R_{\nu\mu}^{-1} \cdot \frac{1}{4n} \sum_{a=1}^{4n} (x_{(a)}^\mu - x_0^\mu) B_i(t_a, r_a). \quad (6)$$

Here, n neighboring measurements from each spacecraft are chosen, totally $N = 4n$ data points included. As shown in Equation A2, the spacetime coordinates at the central point are $x_c^i = \frac{1}{N} \sum_{a=1}^N x_a^i$ and $x_c^4 = \frac{1}{N} \sum_{a=1}^N x_a^4$ or $t_c = \frac{1}{N} \sum_{a=1}^N t_a$. The barycenter coordinates (Harvey, 1998) have been used, so that $x_c^i = 0$ constantly. $R_{\nu\mu}^{-1}$ is the inverse of the general volume tensor $R^{\mu\nu}$ with the definition $R^{\mu\nu} \equiv \frac{1}{N} \sum_{a=1}^N (x_{(a)}^\mu - x_c^\mu)(x_{(a)}^\nu - x_c^\nu)$ as shown in Equation A9.

The above Equations 5 and 6 in the vector format are

$$\mathbf{B}(t_c, r_c) = \frac{1}{4n} \sum_{a=1}^{4n} \mathbf{B}(t_a, r_a), \quad (7)$$

$$\nabla_v \mathbf{B}(t_c, r_c) = R_{\nu\mu}^{-1} \cdot \frac{1}{4n} \sum_{a=1}^{4n} (x_{(a)}^\mu - x_0^\mu) \mathbf{B}(t_a, r_a). \quad (8)$$

These equations will yield the time series of magnetic field $\mathbf{B}(t_c, r_c)$, its time derivative $\partial_t \mathbf{B}(t_c, r_c)$ and first order gradient $\nabla \mathbf{B}(t_c, r_c)$ at the barycenter of the S/C constellation.

In the above Equations 5–8, the accuracy is found to first order due to omission of the second order gradients. We will correct the magnetic field and its first order derivatives at the barycenter with the second order derivatives of the magnetic field according to Appendix A and will further obtain the corrected quadratic magnetic gradient by iteration (see (vii) later). The corrected magnetic field and its first order gradient at the barycenter will then have second order accuracy.

In this investigation, we have neglected the magnetic gradients with orders higher than two, so that the current density can be regarded as linearly varying. According to Equations A14 and A15 in Appendix A, the current density at the barycenter is

$$\mathbf{j}_c = \mathbf{j}(t_c, r_c) = \frac{1}{4n} \sum_{a=1}^{4n} \mathbf{j}(t_a, r_a), \quad (9)$$

and the linear gradient of the current density at the barycenter is

$$\nabla_v \mathbf{j}(t_c, r_c) = R_{\nu\mu}^{-1} \cdot \frac{1}{4n} \sum_{a=1}^{4n} (x_{(a)}^\mu - x_0^\mu) \mathbf{j}(t_a, r_a), \quad (10)$$

of which the component form is

$$\nabla_v j_k(t_c, r_c) = R_{\nu\mu}^{-1} \cdot \frac{1}{4n} \sum_{a=1}^{4n} (x_{(a)}^\mu - x_0^\mu) j_k(t_a, r_a). \quad (10a)$$

Generally, the electron and ion measurements have different time resolutions. So that the electron and ion current densities and their linear gradients at the barycenter can be first calculated separately with Equations 9 and 10, and finally added to obtain the total current density and its linear gradient at the barycenter.

- (ii) The second order time derivative of the magnetic field and the first order time derivative of the magnetic gradient

With the time series of magnetic field $\mathbf{B}(t_c, \mathbf{r}_c)$ and its first order time derivative $\partial_t \mathbf{B}(t_c, \mathbf{r}_c)$ at the barycenter obtained in (i), it is easy to get the second order time derivative of magnetic field $\partial_t \partial_t \mathbf{B}(t_c, \mathbf{r}_c)$ at the barycenter, where $\partial_t \equiv \partial / \partial t$.

The gradient of the time derivative of the magnetic field is equivalent to the time derivative of the magnetic gradient, that is,

$$\nabla_j \partial_t B_i(t, \mathbf{r}) = \partial_t \left[\nabla_j B_i(t, \mathbf{r}) \right]. \quad (11)$$

Therefore, at the central point (t_c, \mathbf{r}_c) ,

$$\nabla_j \partial_t B_i(t_c, \mathbf{r}_c) = \partial_t \nabla_j B_i(t_c, \mathbf{r}_c) = \frac{\partial}{\partial t_c} \left[\nabla_j B_i(t_c, \mathbf{r}_c) \right]. \quad (12)$$

- (iii) The transformations between the temporal and spatial gradients of the magnetic field in different reference frames

This approach will make use of the proper reference frame of the magnetic structure, so as to determine the second order gradient in the direction of the apparent motion of the magnetic structure, that is, the longitudinal quadratic gradient of the magnetic field. To do this, we need to find the apparent velocity V of the magnetic structure relative to the spacecraft constellation. For space plasmas, this relative velocity is much less than the speed of the light in vacuum, that is, $V \ll c$. Shi et al. (2006) have first obtained the velocity of the magnetic structure relative to the spacecraft with the temporal and spatial variation rates of the magnetic field under the assumption of stationarity. Hamrin et al. (2008) have obtained the apparent velocity of the magnetic structure using a proper reference frame. Here we give a concise discussion on the transformations between the temporal and spatial gradients of the magnetic field in different reference frames.

The time and space coordinates (t, \mathbf{r}) in the S/C constellation reference frame and the corresponding time and space coordinates (t', \mathbf{r}') in the proper reference frame of the magnetic structure obey the Galilean transformations, that is, $t' = t$, $\mathbf{r}' = \mathbf{r} - V\mathbf{t}$ (see also Figure 1) (The Eulerian description is applied in each reference frame.). The magnetic fields observed in the S/C constellation frame and the proper frame of the magnetic structure are $\mathbf{B}(t, \mathbf{r})$ and $\mathbf{B}'(t', \mathbf{r}')$, respectively. As $V \ll c$, $\mathbf{B}(t, \mathbf{r}) = \mathbf{B}'(t', \mathbf{r}')$. It is obvious that the magnetic gradient in these two reference frames are also identical, that is,

$$\nabla \mathbf{B}(t, \mathbf{r}) = \nabla' \mathbf{B}'(t', \mathbf{r}'). \quad (13)$$

The relationship between the time derivative of the magnetic field in the S/C constellation, $\frac{\partial \mathbf{B}(t, \mathbf{r})}{\partial t}$, and time derivative of the magnetic field in the proper reference frame of the magnetic structure, $\frac{\partial \mathbf{B}'(t', \mathbf{r}')}{\partial t'}$, is

$$\frac{\partial \mathbf{B}(t, \mathbf{r})}{\partial t} = \frac{\partial \mathbf{B}'(t', \mathbf{r}')}{\partial t} = \frac{\partial t'}{\partial t} \frac{\partial \mathbf{B}'(t', \mathbf{r}')}{\partial t'} + \frac{\partial \mathbf{r}'}{\partial t} \cdot \nabla' \mathbf{B}'(t', \mathbf{r}'),$$

or

$$\frac{\partial \mathbf{B}(t, \mathbf{r})}{\partial t} = \frac{\partial \mathbf{B}'(t', \mathbf{r}')}{\partial t'} - V \cdot \nabla \mathbf{B}(t, \mathbf{r}). \quad (14)$$

which is the same formula as given by Song and Russell (1999) and Shi et al. (2006).

In the proper reference frame of the magnetic structure, $\frac{\partial \mathbf{B}'(t', \mathbf{r}')}{\partial t'} = 0$, thus

$$\frac{\partial \mathbf{B}(t, \mathbf{r})}{\partial t} = -V(t, \mathbf{r}) \cdot \nabla \mathbf{B}(t, \mathbf{r}). \quad (15)$$

At the barycenter of the S/C constellation,

$$\frac{\partial \mathbf{B}(t, \mathbf{r}_c)}{\partial t} = -\mathbf{V}(t, \mathbf{r}_c) \cdot \nabla \mathbf{B}(t, \mathbf{r}_c). \quad (16)$$

The component form of the above formula is

$$\frac{\partial B_j(t, \mathbf{r}_c)}{\partial t} = -V_i(t, \mathbf{r}_c) \cdot \nabla_i B_j(t, \mathbf{r}_c). \quad (16a)$$

The above equation has a unique solution of the apparent velocity and a proper reference frame can be found only if $|\nabla \mathbf{B}(t, \mathbf{r})| \neq 0$. Thus the apparent velocity of the magnetic structure relative to the S/C constellation is (Hamrin et al., 2008; Shi et al., 2006)

$$V_i(t, \mathbf{r}_c) = -V'_i(t, \mathbf{r}_c) = -\partial_i B_j(t, \mathbf{r}_c) \cdot (\nabla \mathbf{B})_{ji}^{-1}(t, \mathbf{r}_c). \quad (17)$$

It is noted that the apparent velocity of the magnetic structure can vary with time. Equation 17 is applicable for magnetic structures with $V \ll c$, whether steady or unsteady.

V can be varying with time. Taking the time derivative of Equation 16, it reduces to

$$\partial_t \partial_i \mathbf{B}(t, \mathbf{r}_c) = -\partial_t \mathbf{V}(t, \mathbf{r}_c) \cdot \nabla \mathbf{B}(t, \mathbf{r}_c) - \mathbf{V}(t, \mathbf{r}_c) \cdot \partial_t \nabla \mathbf{B}(t, \mathbf{r}_c).$$

Then

$$\partial_t \mathbf{V}(t, \mathbf{r}_c) \cdot \nabla \mathbf{B}(t, \mathbf{r}_c) = -\partial_t \partial_i \mathbf{B}(t, \mathbf{r}_c) - \mathbf{V}(t, \mathbf{r}_c) \cdot \partial_t \nabla \mathbf{B}(t, \mathbf{r}_c). \quad (18)$$

Because $\partial_t \partial_i \mathbf{B}(t, \mathbf{r}_c)$ and $\partial_t \nabla \mathbf{B}(t, \mathbf{r}_c)$ have been yielded in (ii), the apparent acceleration $\partial_t \mathbf{V}(t, \mathbf{r}_c)$ of the structure as viewed in the constellation reference frame can be readily obtained.

\mathbf{V} / V is a characteristic, directional vector, so that we can define $-\mathbf{V} / V$ as the directional vector of the x_3 axis in the S/C constellation reference frame, that is, $\hat{x}_3 = -\mathbf{V} / V$.

We can further investigate the transformation between the time derivatives of the magnetic gradients in the two different reference frames. Similarly to the linear magnetic gradients in Equation 13, the quadratic magnetic gradients in the S/C constellation frame and the proper frame of the magnetic structure are identical, that is,

$$\nabla \nabla \mathbf{B}(t, \mathbf{r}) = \nabla' \nabla' \mathbf{B}'(t', \mathbf{r}'). \quad (19)$$

The relationship between the time derivative of the magnetic gradient in the S/C constellation frame, $\partial_t \nabla \mathbf{B}(t, \mathbf{r})$, and the time derivative of the magnetic gradient in the proper frame of the magnetic structure, $\partial_{t'} \nabla' \mathbf{B}'(t', \mathbf{r}')$, satisfies

$$\begin{aligned} \frac{\partial}{\partial t} \nabla \mathbf{B}(t, \mathbf{r}) &= \frac{\partial}{\partial t} \nabla' \mathbf{B}'(t', \mathbf{r}') \\ &= \frac{\partial t'}{\partial t} \frac{\partial}{\partial t'} \nabla' \mathbf{B}'(t', \mathbf{r}') + \frac{\partial \mathbf{r}'}{\partial t} \cdot \nabla' \nabla' \mathbf{B}'(t', \mathbf{r}') \\ &= \nabla' \frac{\partial}{\partial t'} \mathbf{B}'(t', \mathbf{r}') - \mathbf{V} \cdot \nabla' \nabla' \mathbf{B}'(t', \mathbf{r}'). \end{aligned}$$

Considering $\frac{\partial \mathbf{B}'(t', \mathbf{r}')}{\partial t'} = 0$ in the proper reference frame and Equation 19, this reduces to

$$\frac{\partial}{\partial t} \nabla \mathbf{B}(t, \mathbf{r}) = -\mathbf{V} \cdot \nabla \nabla \mathbf{B}(t, \mathbf{r}), \quad (20)$$

which is the formula relating the time derivative of the linear magnetic gradient to the quadratic magnetic gradient in the S/C constellation reference frame. With this general formula the gradient of the linear magnetic gradient in the direction of apparent velocity is readily obtained as shown below in (iv).

(iv) The longitudinal gradient of $\nabla \mathbf{B}(t, \mathbf{r}_c)$

Based on Equation 20, the gradient of the linear magnetic gradient along the x_3 direction at the barycenter \mathbf{r}_c satisfies

$$V \frac{\partial}{\partial x^3} \nabla \mathbf{B}(t, \mathbf{r}_c) = \partial_t \nabla \mathbf{B}(t, \mathbf{r}_c), \quad (21)$$

or

$$\partial_3 \partial_k B_m(t, \mathbf{r}_c) = \frac{1}{V} \partial_t \partial_k B_m(t, \mathbf{r}_c). \quad (22)$$

The right hand side of the above equation can be obtained from Equation 12, so that nine components of the quadratic magnetic gradient can be obtained. Formula 22 is applicable for both steady and unsteady magnetic structures.

Furthermore, due to the symmetry of the quadratic gradient,

$$\nabla_p \nabla_3 B_l = \nabla_3 \nabla_p B_l, \quad (23)$$

of which the right hand side is given by Equation 20, so that 6 more components of the quadratic magnetic gradient can be obtained. Now only $\nabla_p \nabla_q B_l(p, q = 1, 2, l = 1, 2, 3)$ are to be found, which involve $4 \times 3 = 12$ components. Considering the symmetry of the quadratic magnetic gradient, $\nabla_p \nabla_q B_l = \nabla_q \nabla_p B_l$, only $3 \times 3 = 9$ of these components are independent.

The gradient of the current density will be needed for the estimation of the remaining components of the quadratic magnetic gradient.

(v) Three components and two constraints for the quadratic magnetic gradient using the gradient of current density

From Ampere's law, we get the constraints that

$$\nabla(\nabla \times \mathbf{B}) = \nabla \mathbf{j},$$

with which we can obtain some components of the quadratic magnetic gradient if $\nabla \mathbf{j}$ is known (for simplicity, we replace $\mu_0 \mathbf{j}$ by \mathbf{j}). If the electromagnetic fields are strongly varying, $\mathbf{j} = \nabla \times \mathbf{B} - c^{-2} \partial \mathbf{E} / \partial t$, with the electric displacement current included. However, in this investigation we only consider the slow-varying electromagnetic fields with the limitation $|\nabla \times \mathbf{B}| \gg c^{-2} |\partial \mathbf{E} / \partial t|$, which is commonly satisfied in large scale space plasmas. The component equation $\partial_3(\nabla \times \mathbf{B}) = \partial_3 \mathbf{j}$ is not an independent constraint due to Equation 22. It is a surplus condition, which we have not used because Equation 22 can yield the longitudinal gradient directly already. Furthermore, $\nabla \cdot \mathbf{j} = \nabla \cdot (\nabla \times \mathbf{B}) = 0$, so that the gradient of the current density only provides $9 - 3 - 1 = 5$ independent constraints.

The transverse quadratic gradient of the longitudinal magnetic field, that is, the quadratic gradient of the magnetic component B_3 in the plane orthogonal to the direction of motion (or x_3 direction) satisfies

$$\partial_p \partial_q B_3 = \partial_p (\partial_q B_3 - \partial_3 B_q + \partial_3 B_q) = \partial_p (\varepsilon_{lq3} j_l + \partial_3 B_q), \quad (24)$$

where again Ampere's law $\nabla \times \mathbf{B} = \mathbf{j}$ has been used. Thus, Equation 24 leads to

$$\partial_p \partial_q B_3(t, \mathbf{r}_c) = \varepsilon_{lq3} \partial_p j_l(t, \mathbf{r}_c) + \partial_3 \partial_p B_q(t, \mathbf{r}_c), \quad (25)$$

where $\partial_p j_q$ is used. The above formula yields the transverse quadratic magnetic gradient of the longitudinal magnetic field and contains three independent components of the quadratic magnetic gradient at the barycenter.

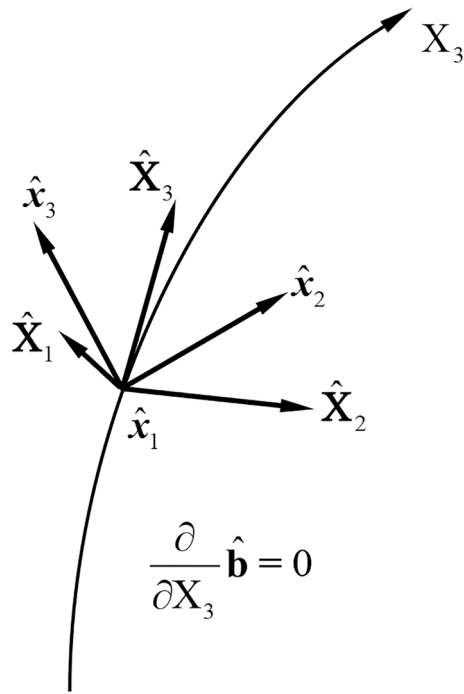


Figure 2. Illustration of the characteristic direction at which the magnetic rotation minimizes.

There are still 6 components of the quadratic magnetic gradient remaining to be determined, that is, $\partial_p \partial_q B_s(t, \mathbf{r}_c)$, which are the transverse quadratic gradients of the transverse magnetic field.

Two additional constraints can be obtained from $\partial_p j_3 = \partial_p (\partial_1 B_2 - \partial_2 B_1)$, ($p, q = 1, 2$), that is,

$$\begin{cases} \partial_1 \partial_1 B_2 - \partial_1 \partial_2 B_1 = \partial_1 j_3 & (26) \\ \partial_2 \partial_1 B_2 - \partial_2 \partial_2 B_1 = \partial_2 j_3 & (27) \end{cases}$$

which is at the barycenter.

Based on Ampere's law, therefore, three more components of the quadratic magnetic gradient and two constraints on it can be obtained with the gradient of current density as shown in Equations 25–27.

Now four constraints are to be found for the complete determination of the quadratic magnetic gradient.

(vi) The last four constraints

The magnetic field is divergence-free, that is, $\nabla \cdot \mathbf{B} = 0$. Therefore

$$\partial_j \partial_k B_k = 0. \quad (28)$$

It is noted that the sum over k is made in the above formula. Because $\partial_3 \partial_k B_k = 0$ is a dependent constraint in Equation 22, there are only two independent constraints, that is, $\partial_p \partial_k B_k = 0$, ($p, q = 1, 2$). So that

$$\partial_1 \partial_1 B_1 + \partial_1 \partial_2 B_2 = -\partial_1 \partial_3 B_3, \quad (29)$$

$$\partial_2 \partial_1 B_1 + \partial_2 \partial_2 B_2 = -\partial_2 \partial_3 B_3, \quad (30)$$

where $\partial_p \partial_3 B_3 = \partial_3 \partial_p B_3 = \frac{1}{V} \partial_p \partial_l B_3$ according to Equation 22.

There are therefore only two constraints left to be found.

Using magnetic rotation analysis (MRA) (Shen et al., 2007, see also Appendix B), the remaining two constraints can be obtained from the properties of the magnetic field. As shown in Appendix B, based on MRA, the magnetic rotation tensor has three characteristic directions ($\hat{\mathbf{X}}_1, \hat{\mathbf{X}}_2, \hat{\mathbf{X}}_3$), as illustrated here in Figure 2. The coordinate line X_3 is along $\hat{\mathbf{X}}_3$. In the third characteristic direction $\hat{\mathbf{X}}_3$, the magnetic unit vector $\hat{\mathbf{b}} = \mathbf{B}/B$ has no rotation, and the square of the magnetic rotation rate is

$$\frac{\partial \hat{\mathbf{b}}}{\partial X_3} \cdot \frac{\partial \hat{\mathbf{b}}}{\partial X_3} = 0. \quad (31)$$

So that

$$\frac{\partial \hat{\mathbf{b}}}{\partial X_3} = 0. \quad (32)$$

Since $\frac{\partial \hat{\mathbf{b}}}{\partial X_3} = 0$ at each point of the coordinate line X_3 (as indicated in Figure 2), we have

$$\frac{\partial}{\partial X_3} \frac{\partial \hat{\mathbf{b}}}{\partial X_3} = 0. \quad (33)$$

Since the magnetic unit vector $\hat{\mathbf{b}}$ obeys $\hat{\mathbf{b}} \cdot \hat{\mathbf{b}} = 1$, the above constraint contains only two independent component equations, which can be chosen as

$$\frac{\partial}{\partial X_3} \frac{\partial B_p}{\partial X_3} \frac{1}{B} = 0, p = 1, 2. \quad (34)$$

The three characteristic directions ($\hat{\mathbf{X}}_1, \hat{\mathbf{X}}_2, \hat{\mathbf{X}}_3$) have a relationship with the base vectors ($\hat{\mathbf{x}}_1, \hat{\mathbf{x}}_2, \hat{\mathbf{x}}_3$) of the S/C coordinates (x_1, x_2, x_3), as follows:

$$\hat{\mathbf{X}}_i = a_{ij}\hat{\mathbf{x}}_j, \quad (35)$$

where the coefficients $a_{ij} = \hat{\mathbf{X}}_i \cdot \hat{\mathbf{x}}_j = \cos[\angle(\hat{\mathbf{X}}_i, \hat{\mathbf{x}}_j)]$. If we assume a vector $\mathbf{X} = x_i\hat{\mathbf{x}}_i = X_j\hat{\mathbf{X}}_j$, then $x_i = X_j\hat{\mathbf{X}}_j \cdot \hat{\mathbf{x}}_i = a_{ji}X_j$.

The first order partial derivative obeys:

$$\frac{\partial}{\partial X_3} = \frac{\partial x_k}{\partial X_3} \cdot \frac{\partial}{\partial x_k} = a_{3k} \frac{\partial}{\partial x_k},$$

and the second order partial derivative obeys:

$$\frac{\partial}{\partial X_3} \frac{\partial}{\partial X_3} = a_{3k} \frac{\partial}{\partial x_k} \left(a_{3j} \frac{\partial}{\partial x_j} \right) = a_{3k} a_{3j} \frac{\partial}{\partial x_k} \frac{\partial}{\partial x_j}.$$

Generally, $\hat{\mathbf{X}}_3$ is varying slowly in space and $\frac{\partial}{\partial x_k} a_{3j}$ is a small quantity, thus $\frac{\partial}{\partial x_k} a_{3j}$ is omitted in the above equations. Therefore, Equation 34 reduces to

$$a_{3k} a_{3j} \frac{\partial}{\partial x^k} \frac{\partial}{\partial x^j} \left(\frac{B_p}{B} \right) = 0, \quad p = 1, 2. \quad (36)$$

Finally, we show below that we can find $\partial_p \partial_q B_s(t, \mathbf{r}_c)$ by combining Equations 26, 27, 29, 30 and 36.

We also can investigate Equation 36 in more detail. For simplicity, we can adjust the coordinates (x_1, x_2, x_3). We keep the x_3 axis unchanged with its basis $\hat{\mathbf{x}}_3 = -V/V$, and rotate x_1 and x_2 axes around the x_3 axis such that the coordinate base vector $\hat{\mathbf{x}}_1$ is orthogonal to both $\hat{\mathbf{x}}_3$ and $\hat{\mathbf{X}}_3$, that is,

$$\hat{\mathbf{x}}_1 = \frac{\hat{\mathbf{X}}_3 \times \hat{\mathbf{x}}_3}{|\hat{\mathbf{X}}_3 \times \hat{\mathbf{x}}_3|}, \quad (37)$$

(and as illustrated in Figure 2). Thus

$$a_{31} = \hat{\mathbf{X}}_3 \cdot \hat{\mathbf{x}}_1 = 0.$$

Then Equation 36 becomes

$$a_{32}^2 \frac{\partial^2}{\partial x_2^2} \left(\frac{B_p}{B} \right) = -a_{33}^2 \frac{\partial^2}{\partial x_3^2} \left(\frac{B_p}{B} \right) - 2a_{33}a_{32} \frac{\partial}{\partial x_3} \frac{\partial}{\partial x_2} \left(\frac{B_p}{B} \right). \quad (38)$$

All the terms in the right hand side of the above equation are known. With Equation 59 developed in the next section, we can express the second order gradients of the components of the magnetic unit vector on the two sides of Equation 38 in terms of the magnetic gradients. With Equation 59, we get

$$\frac{\partial}{\partial x_2} \frac{\partial}{\partial x_2} \left(\frac{B_p}{B} \right) = B^{-1} \partial_2 \partial_2 B_p - B^{-3} B_p B_i \partial_2 \partial_2 B_i - 2B^{-2} \partial_2 B_p \partial_2 B + 3B^{-3} B_p \partial_2 B \partial_2 B - B^{-3} B_p \partial_2 B_i \partial_2 B_i, \quad (39)$$

or

$$\begin{aligned} \partial_2 \partial_2 \left(\frac{B_p}{B} \right) &= \left(B^{-1} \partial_2 \partial_2 B_p - B^{-3} B_p B_s \partial_2 \partial_2 B_s \right) \\ &+ \left(-B^{-3} B_p B_3 \partial_2 \partial_2 B_3 - 2B^{-2} \partial_2 B_p \partial_2 B + 3B^{-3} B_p \partial_2 B \partial_2 B - B^{-3} B_p \partial_2 B_i \partial_2 B_i \right). \end{aligned} \quad (39a)$$

The second expression on the right hand side is known already. Substituting (39a) into (38), we get

$$B^{-1}\partial_2\partial_2B_p - \sum_{s=1}^2 B^{-3}B_pB_s\partial_2\partial_2B_s = -\frac{a_{33}^2}{a_{32}^2}\frac{\partial^2}{\partial x_3^2}\left(\frac{B_p}{B}\right) - \frac{2a_{33}}{a_{32}}\partial_3\partial_2\frac{B_p}{B} - \left[-B^{-3}B_pB_3\partial_2\partial_2B_3 - 2B^{-2}\partial_2B_p\partial_2B + 3B^{-3}B_p\partial_2B\partial_2B - B^{-3}B_p\partial_2B_i\partial_2B_i\right] \quad (40)$$

where $p = 1, 2$. All the terms in the right hand side of the above equation can be determined with (59), (8), (22), (23), and (24).

Therefore, combining Equations 26, 27, 29, 30 and 40, we can determine $\partial_p\partial_qB_s(t, \mathbf{r}_c)$.

Actually, with the two equations in Equation 40, we can completely find the solution $\partial_2\partial_2B_s(t, \mathbf{r}_c)$, ($s = 1, 2$).

Furthermore, with Equations 30 and 27, we can get $\partial_1\partial_2B_s(t, \mathbf{r}_c)$, ($s = 1, 2$), that is,

$$\partial_1\partial_2B_1 = \partial_2\partial_1B_1 = -\partial_2\partial_2B_2 - \partial_2\partial_3B_3, \quad (41)$$

and

$$\partial_1\partial_2B_2 = \partial_2\partial_1B_2 = \partial_2\partial_2B_1 + \partial_2j_3. \quad (42)$$

The above two equations are valid at the barycenter.

In addition, from Equations 29 and 26, we can obtain $\partial_1\partial_1B_s(t, \mathbf{r}_c)$, ($s = 1, 2$), that is,

$$\partial_1\partial_1B_1 = -\partial_1\partial_2B_2 - \partial_1\partial_3B_3, \quad (43)$$

and

$$\partial_1\partial_1B_2 = \partial_1\partial_2B_1 + \partial_1j_3. \quad (44)$$

The above two equations are also valid at the barycenter.

So far, we have obtained all the components of the quadratic gradient $(\nabla\nabla\mathbf{B})_c$ at the barycenter. The accuracy of the quadratic gradient is to first order, just as that for the magnetic gradient.

(vii) Recalculating the magnetic gradients by iteration

In order to enhance the accuracy of the magnetic quantities, we can correct the estimate of the field and its linear gradient at the barycenter with the quadratic magnetic gradient obtained above (based on Equations A8 and A13 in Appendix A). Subsequently, we can further go through the above steps (ii-vi) to get the corrected quadratic magnetic gradient with better accuracy.

The procedure is as follows:

By Taylor expansion as in Equation A3, the magnetic fields measured by the four spacecraft are

$$B_i(t_a, \mathbf{r}_a) = B_i(t_c, \mathbf{r}_c) + \Delta x_{(a)}^v \nabla_v B_i(t_c, \mathbf{r}_c) + \frac{1}{2} \Delta x_{(a)}^v \Delta x_{(a)}^\lambda \nabla_v \nabla_\lambda B_i(t_c, \mathbf{r}_c). \quad (45)$$

Based on Equation A8 in Appendix A, we obtain the magnetic field at the barycenter, corrected by the quadratic magnetic gradient, as:

$$B_i(t_c, \mathbf{r}_c) = \frac{1}{4n} \sum_{a=1}^{4n} B_i(t_a, \mathbf{r}_a) - \frac{1}{2} R^{\nu\lambda} \nabla_v \nabla_\lambda B_i(t_c, \mathbf{r}_c), \quad (46)$$

where, the general volume tensor $R^{\nu\lambda}$ is as defined in Equation A9.

From Equation A13 in Appendix A, we get the first order magnetic gradient at the barycenter corrected from the quadratic magnetic gradient as

$$\nabla_v B_i(t_c, \mathbf{r}_c) = (\mathbf{R}^{-1})_{\nu\mu} \cdot \frac{1}{N} \sum_a^N (x_{(a)}^\mu - x_c^\mu) B_i(t_a, \mathbf{r}_a) - \frac{1}{2} (\mathbf{R}^{-1})_{\nu\mu} R^{\mu\sigma\lambda} \nabla_\sigma \nabla_\lambda B_i(t_c, \mathbf{r}_c). \quad (47)$$

Furthermore, we can perform the above steps (ii–vi) to obtain the corrected quadratic magnetic gradient using these updated estimates. The quadratic magnetic gradient obtained in this iterative sense has a higher accuracy, while errors in the magnetic field, its linear gradient and the apparent velocity of the magnetic structure at the barycenter, are of second order in L/D , where L is the size of the S/C constellation and D is the characteristic scale of the magnetic structure.

We can call this new method as Nonlinear Magnetic Gradient (NMG) algorithm for convenience.

To summarize the NMG algorithm, we proceed as follows

- (a) Estimate the magnetic field \mathbf{B}_c ; the first order magnetic gradient $(\nabla\mathbf{B})_c$, and the time variation rate $\left(\frac{\partial\mathbf{B}}{\partial t}\right)_c$ of the magnetic field, at the barycenter and under the linear approximation; as in Equations 7 and 8. Estimate the gradient of the current density at the barycenter $\nabla\mathbf{j}(t, \mathbf{r}_c)$, as in Equation 10.
- (b) Determine the apparent velocity V using the time variation rate $\left(\frac{\partial\mathbf{B}}{\partial t}\right)_c$ of the magnetic field and the first order magnetic gradient $(\nabla\mathbf{B})_c$ with Equation 16a or 17 and define the x_3 coordinate with $\hat{\mathbf{x}}_3 = -V / V$; determine the three characteristic directions $(\hat{\mathbf{X}}_1, \hat{\mathbf{X}}_2, \hat{\mathbf{X}}_3)$ using MRA, and define the coordinate base vector $\hat{\mathbf{x}}_1 = \frac{\hat{\mathbf{X}}_3 \times \hat{\mathbf{x}}_3}{|\hat{\mathbf{X}}_3 \times \hat{\mathbf{x}}_3|}$, such as to fix the Cartesian coordinates (x_1, x_2, x_3) in the spacecraft constellation reference frame.
- (c) Calculate the time variation rate $\frac{\partial}{\partial t}(\nabla\mathbf{B})_c$ of the linear magnetic gradient at the barycenter, so as to obtain the components of the quadratic magnetic gradient $(\nabla_3\nabla\mathbf{B})_c$ and $(\nabla\nabla_3\mathbf{B})_c$, as in Equations 22 and 23.
- (d) Combine Ampere's law and the first order gradient of the current density $\nabla\mathbf{j}(t, \mathbf{r}_c)$ to calculate the transverse quadratic gradient of B_3 , that is, $\nabla_p\nabla_q B_3(p, q = 1, 2)$, as in Equation 25.
- (e) Solve the equations $\frac{\partial}{\partial X_3} \frac{\partial}{\partial X_3} \hat{\mathbf{b}} = 0$, or Equation 38 equivalently, derived by MRA, so as to obtain the components: $\partial_2\partial_2 B_p(p = 1, 2)$.
- (f) Determine the remaining four components of the quadratic magnetic gradient, $(\partial_1\partial_2 B_p)_c = (\partial_2\partial_1 B_p)_c$ and $(\partial_1\partial_1 B_p)_c(p = 1, 2)$, using the equation $\nabla(\nabla \cdot \mathbf{B}) = 0$ derived from the divergence free condition of the magnetic field and the equation $\nabla(\nabla \times \mathbf{B}) = \nabla\mathbf{j}$ from Ampere's law, as in Equations 41–44.
- (g) Revise the magnetic field \mathbf{B}_c and the first order magnetic gradient $(\nabla\mathbf{B})_c$ with the quadratic magnetic gradient $G^{(2)} = (\nabla\nabla\mathbf{B})_c$ obtained initially, as in Equations 46 and 47, and perform the above steps (b–f) once again, so as to get the corrected quadratic magnetic gradient $(\nabla\nabla\mathbf{B})_c$, as well as the corrected apparent velocity V of the magnetic structure.

It should be noted that the magnetic field, the linear magnetic gradient and the quadratic magnetic gradient are all identical in different reference frames. We will test all these estimators in detail in Section 4.

Given the magnetic field \mathbf{B}_c , the first order magnetic gradient $(\nabla\mathbf{B})_c$ and the quadratic magnetic gradient $(\nabla\nabla\mathbf{B})_c$, the complete geometry of the magnetic field lines of the magnetic structure can be determined. We will find the estimators for the geometrical parameters of the MFLs in the next section.

3. Determining the Complete Geometry of Magnetic Field Lines Based on Multiple S/C Measurements

The geometry of the MFLs plays a critical role in the evolution of the space plasmas. In this section, we will extract the estimators for the complete geometry of the MFLs, from the linear and quadratic gradients of the magnetic field estimated in Section 2.

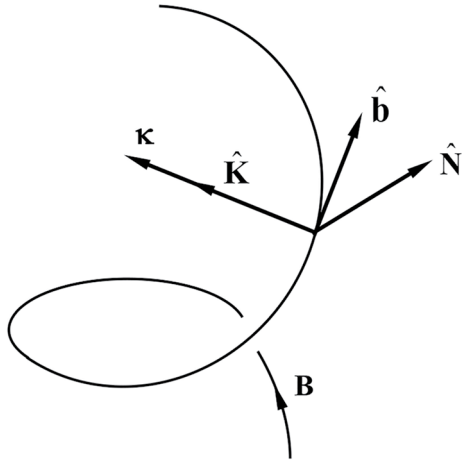


Figure 3. Demonstration on the geometry of the magnetic field lines. $\hat{\mathbf{b}} = \mathbf{B} / B$ is the magnetic unit vector; $\boldsymbol{\kappa}$ is the curvature vector of the magnetic field line, $\hat{\mathbf{K}}$ and $\hat{\mathbf{N}}$ are the principal normal and binormal, respectively. The magnetic field line is also twisting with torsion.

3.1. The Natural Coordinates and Curvature of the MFLs

The geometry of the magnetic field lines is illustrated in Figure 3. The directional magnetic unit vector is $\hat{\mathbf{b}} = \mathbf{B} / B$, which is also the tangential vector of the MFLs. The MFLs are usually turning, and the bending of MFLs is characterized by the curvature vector, that is,

$$\boldsymbol{\kappa} = \frac{d\hat{\mathbf{b}}}{ds} = (\hat{\mathbf{b}} \cdot \nabla)\hat{\mathbf{b}}, \quad (48)$$

where “s” is the arc length along the MFLs.

Shen et al. (2003, 2011) first presented the estimator of the curvature of MFLs, which has found many applications in multi-point data analysis. Here, a brief description of it is given and we will then investigate further the complete geometry of the MFLs as well as the explicit estimators.

The gradient of the magnetic field $(\nabla \mathbf{B})_c$ at the barycenter from multi-spacecraft measurements has already been expressed in Section 2.

The gradient of the magnetic strength $B = |\mathbf{B}|$ is

$$\nabla_i B = \frac{1}{2B} \nabla_i B^2 = \frac{1}{B} B_j \nabla_i B_j, \quad (49)$$

while at the barycenter of the S/C constellation,

$$(\nabla_i B)_c = B_c^{-1} B_{cj} (\nabla_i B_j)_c. \quad (50)$$

Similarly, the gradient of the unit magnetic vector $\hat{\mathbf{b}}$ is

$$\nabla_i b_j = \nabla_i \frac{B_j}{B} = B^{-1} \nabla_i B_j - B^{-2} B_j \nabla_i B. \quad (51)$$

with Equation 49, the above Equation 51 becomes

$$\nabla_i b_j = B^{-1} \nabla_i B_j - B^{-1} b_j b_m \nabla_i B_m. \quad (52)$$

Hence, the gradient of the unit magnetic vector $\hat{\mathbf{b}}$ at the barycenter is

$$(\nabla_i b_j)_c = B^{-1} (\nabla_i B_j)_c - B^{-1} b_j b_m (\nabla_i B_m)_c. \quad (53)$$

All the coefficients on the right hand side of the above formula involve values at the barycenter (Shen, et al., 2003): $(B_i)_c = \frac{1}{N} \sum_{\alpha=1}^N B_{\alpha i}$, $(b_i)_c = B_{ci} / |B_c|$. Equation 53 obeys the condition that: $b_j (\nabla_i b_j)_c = 0$, which is required by the constraint $\hat{\mathbf{b}} \cdot \hat{\mathbf{b}} = 1$.

The curvature of the MFLs at the barycenter is therefore

$$\kappa_{cj} = b_i (\nabla_i b_j)_c = B^{-1} b_i (\nabla_i B_j)_c - B^{-1} b_i b_j b_m (\nabla_i B_m)_c. \quad (54)$$

All the coefficients on the right hand side of the above formula involve values at the barycenter. Equation 54 is the estimator of the curvature of the MFLs based on the multi-S/C magnetic measurements. It is noted that there can be no field line crossing through the point where $B = 0$; thus, there is no need to calculate the curvature from Equation 54. It is noted that Equation 54 satisfies $\hat{\mathbf{b}}_c \cdot \boldsymbol{\kappa}_c = b_{cj} \kappa_{cj} = 0$, indicating that the obtained curvature vector is orthogonal to the magnetic field.

The radius of the curvature of the MFLs is

$$R_c = 1 / \kappa_c. \quad (55)$$

The principal normal vector of the MFLs is

$$\hat{\mathbf{K}} = \boldsymbol{\kappa}_c / |\boldsymbol{\kappa}_c|. \quad (56)$$

The binormal vector of the MFLs is

$$\hat{\mathbf{N}} = \hat{\mathbf{b}} \times \hat{\mathbf{K}} = \frac{\hat{\mathbf{b}} \times \boldsymbol{\kappa}_c}{\kappa_c}, \quad (57)$$

The above expressions collectively describe the estimators of the magnetic curvature analysis approach (Shen et al., 2003, 2011), where $\{\hat{\mathbf{b}}, \hat{\mathbf{K}}, \hat{\mathbf{N}}\}$ constitute the natural coordinates, or the Frenet frame (trihedron). The unit magnetic vector $\hat{\mathbf{b}}$, principal normal $\hat{\mathbf{K}}$, and binormal $\hat{\mathbf{N}}$ are orthogonal to each other.

Usually, the MFLs not only bend, but also twist, such as the helical MFLs manifested in a flux rope. The twisting of the magnetic field is closely related to the magnetic helicity of the global magnetic structure, which is generally conserved in space (Berger, 1999). The local twist of the MFLs can be described quantitatively by the torsion. In order to get the complete geometry of the MFLs, therefore, the torsion should be known. The torsion of the MFLs is defined as

$$\tau \equiv \frac{1}{\kappa} \frac{d^2 \hat{\mathbf{b}}}{ds^2} \cdot \hat{\mathbf{N}} = \frac{1}{\kappa} \frac{d\boldsymbol{\kappa}}{ds} \cdot \hat{\mathbf{N}} = -\frac{1}{\kappa} \boldsymbol{\kappa} \cdot \frac{d\hat{\mathbf{N}}}{ds}. \quad (58)$$

Therefore, the quadratic gradient of the magnetic field $\nabla \nabla \mathbf{B}$ is essential for the calculation of the torsion of the MFLs.

We now investigate the relationship between the torsion of the MFLs and the quadratic gradient of the unit magnetic vector $\nabla \nabla \hat{\mathbf{b}}$; as well as with the quadratic magnetic gradient $\nabla \nabla \mathbf{B}$.

To do this, we need to first deduce the expression of the quadratic gradient of the unit magnetic vector in terms of the linear and quadratic magnetic gradients.

The quadratic gradient of the unit magnetic vector $\hat{\mathbf{b}}$ is

$$\begin{aligned} \nabla_k \nabla_i b_j &= \nabla_k \left(B^{-1} \nabla_i B_j - B^{-1} b_j b_i \nabla_i B_1 \right) \\ &= \nabla_k B^{-1} \cdot \nabla_i B_j + B^{-1} \nabla_k \nabla_i B_j - \nabla_k \left(B^{-1} b_j b_i \right) \cdot \nabla_i B_1 - B^{-1} b_j b_i \nabla_k \nabla_i B_1 \\ &= -B^{-2} \nabla_k B \cdot \nabla_i B_j + B^{-1} \nabla_k \nabla_i B_j + B^{-2} \nabla_k B \cdot b_j b_i \nabla_i B_1 \\ &\quad - B^{-1} b_i \nabla_k b_j \cdot \nabla_i B_1 - B^{-1} b_j \nabla_k b_i \cdot \nabla_i B_1 - B^{-1} b_j b_i \nabla_k \nabla_i B_1 \\ &= -B^{-2} \nabla_k B \cdot \nabla_i B_j + B^{-1} \nabla_k \nabla_i B_j + 3B^{-2} b_j b_i \nabla_k B \nabla_i B_1 \\ &\quad - B^{-2} b_i \nabla_k B_j \nabla_i B_1 - B^{-2} b_j \nabla_k B_i \cdot \nabla_i B_1 - B^{-1} b_j b_i \nabla_k \nabla_i B_1. \end{aligned} \quad (59)$$

Thus, the estimator of the quadratic gradient of $\hat{\mathbf{b}}$ at the barycenter is expressed as

$$\begin{aligned} \left(\nabla_k \nabla_i b_j \right)_c &= -B^{-2} \left(\nabla_k B \right)_c \left(\nabla_i B_j \right)_c + 3B^{-2} b_j b_m \left(\nabla_k B \right)_c \left(\nabla_i B_m \right)_c - B^{-2} b_m \left(\nabla_k B_j \right)_c \left(\nabla_i B_m \right)_c \\ &\quad - B^{-2} b_j \left(\nabla_k B_m \right)_c \cdot \left(\nabla_i B_m \right)_c + B^{-1} \left(\nabla_k \nabla_i B_j \right)_c - B^{-1} b_j b_m \left(\nabla_k \nabla_i B_m \right)_c. \end{aligned} \quad (60)$$

Based on this definition, the torsion of the MFLs is

$$\begin{aligned} \tau &= \frac{1}{\kappa} \frac{d''}{ds} \cdot \hat{\mathbf{N}} = \frac{1}{\kappa} b_j \partial_j \left(b_k \partial_k b_i \right) N_i \\ &= \frac{1}{\kappa} \left(b_j \partial_j b_k \cdot \partial_k b_i + b_j b_k \partial_j \partial_k b_i \right) N_i. \end{aligned} \quad (61)$$

So that the torsion of the MFLs at the barycenter of the S/C constellation is

$$\tau_c = \kappa^{-1} N_i \cdot \left[b_j \left(\partial_j b_k \right)_c \cdot \left(\partial_k b_i \right)_c + b_j b_k \left(\partial_j \partial_k b_i \right)_c \right]. \quad (62)$$

The above formula is one of the estimators of the torsion of the MFLs that is dependent on the linear and quadratic gradients of the unit magnetic vector $\hat{\mathbf{b}}$.

By substituting Equations 52 and 59 into Equation 61, the torsion of the MFLs is obtained as

$$\tau = \kappa^{-1} B^{-3} N_j B_i \partial_i B_k \partial_k B_j + \kappa^{-1} B^{-3} N_j B_k B_i \partial_k \partial_i B_j, \quad (63)$$

where the condition $b_j N_j = 0$ has been used. Appendix C presents another verification of the expression (63) for clarity. It seems that Equation 63 is invalid as $B = 0$ or $\kappa = 0$. However, there is no field line as $B = 0$, while for $\kappa = 0$, the field line is a straight line and its torsion has no fixed value, and thus is meaningless.

Therefore, the torsion of the MFLs at the barycenter can be written as

$$\tau_c = \kappa^{-1} B^{-3} N_j B_i (\partial_i B_k)_c (\partial_k B_j)_c + \kappa^{-1} B^{-3} N_j B_k B_i (\partial_k \partial_i B_j)_c. \quad (64)$$

All the coefficients on the right hand side of the above formula involve values at the barycenter. Equation 64 is another estimator of the torsion of the MFLs, expressed in terms of the linear and quadratic gradients of the magnetic field. The two different estimators of the torsion of the MFLs (62) and (64) are obviously equivalent.

4. Demonstrations

In this section, the estimators put forward in Sections 2 and 3 will be demonstrated for model current sheets and flux ropes, which can occur in the magnetosphere, in order to verify the validity and accuracy of this approach. A one-dimensional Harris current sheet model (Harris, 1962) and a Lundquist-Lepping cylindrical force-free flux rope model (Lundquist, 1950) are used for these two typical structures, respectively. Appendices D and E present, analytically, the geometrical features of these two kinds of magnetic structures. The tests below have shown that the estimators of the quadratic magnetic gradients and the complete geometry of the MFLs are obtained with good accuracy compared to the models, so we expect they can find wide applications in investigating the magnetic structures and configurations in space plasmas with multi-S/C measurements.

The operative calculating steps can follow the steps (a–g) summarized at the end part of Section 2. The curvature and torsion of magnetic field lines can be obtained by Equations 54 and 64 (or 62) in Section 3.

4.1. One-Dimensional Harris Current Sheet

For the one-dimensional Harris current sheet, the magnetic field can be formulated as Equation (D1) in Appendix D. In this test, the parameters of the current sheet are $B_0 = 50\text{nT}$, $B_y = 10\text{nT}$, $B_z = 20\text{nT}$, $h = R_E$. As shown in Figure 4a, we set an arbitrary S/C constellation trajectory from (2, 2, 2) R_E to (−2, −2, −2) R_E during 100 s. The S/C constellation is assumed to be a regular tetrahedron with a separation of $L = 100$ km. The analytic values of the magnetic field and the current density at the barycenter of the four S/Cs are shown in panels (b) and (c) in Figure 4, respectively.

In this test, we have set $n = 10$, and make $N = 4n = 40$ points to calculate the spatial and temporal gradient of the magnetic field at the barycenter of the S/C constellation with the method in Appendix A. Therefore, we can get the spatial gradient of the vector field within the interval 5–95 s. Furthermore, the temporal and spatial scale corresponds to the time resolution of the field sampling (i.e., $T = 1\text{s}$) and the characteristic size of tetrahedron ($L = 100$ km). The magnetic field and the nonzero component $\frac{\partial B_x}{\partial z}$ of the linear magnetic gradient at the barycenter are derived with Equations 5 and 6 and shown in Figures 4b and 4d, respectively, which are in good agreement with their analytic values as given by Appendix A (the circles represent the results derived by the method, while the black solid line denotes the analytic results derived by theoretical formula). The current density at the barycenter can also be derived with $\frac{\partial B_x}{\partial z}$ by Ampere's law ($\mathbf{j} = \nabla \times \mathbf{B}$) and is shown in Figure 4c. Those values are again consistent with the analytic values. The apparent velocity of the current sheet relative to the S/C constellation can be derived by Equation 15. As shown in Figure 4e, the velocity V_z of S/C relative to the current sheet is within the range 252 ~ 260 km/s (0.0408 ~ 0.0398 Re/s), while the actual velocity is 257 km/s (0.0404 Re/s). Thus, the maximum relative error of the deduced velocity is $\frac{0.0006}{0.0404} \approx 1.5\%$, which is approximately the order of L/h (~ 0.016).

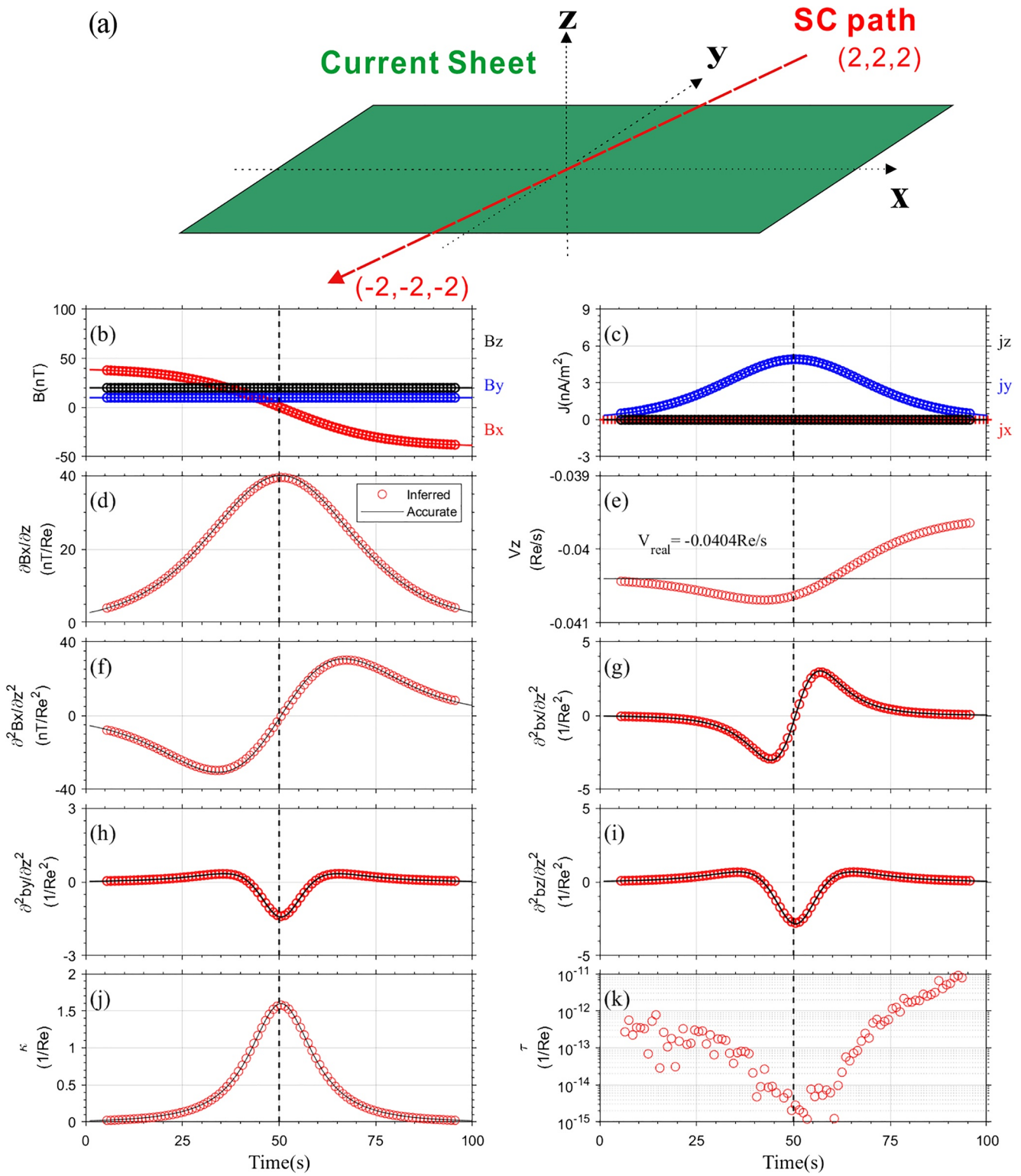


Figure 4.

With the derived linear magnetic gradient and current density gradient, the quadratic magnetic gradient of this current sheet model can be readily obtained. It should be noted that, among the components of the quadratic magnetic gradient, only $\frac{\partial^2 B_x}{\partial z^2}$ is nonzero, while $\frac{\partial^2 b_x}{\partial z^2}$, $\frac{\partial^2 b_y}{\partial z^2}$, $\frac{\partial^2 b_z}{\partial z^2}$ are nonzero among the components of the quadratic gradient of magnetic unit vectors. The test is therefore focused on these components. Evidently, from Figures 4g–4j, there is extremely good agreement between the results obtained by the technique and the analytic values. As illustrated in Figure 4, $\frac{\partial^2 B_x}{\partial z^2}$ (Figure 4f) and $\frac{\partial^2 b_x}{\partial z^2}$ (Figure 4g) have bipolar signatures around the center of current sheet and are equal to zero at the center, while $\frac{\partial^2 b_y}{\partial z^2}$ (Figure 4h) and $\frac{\partial^2 b_z}{\partial z^2}$ (Figure 4i) show left-right symmetry around the current sheet center and reach a minimum at the center. These results are reasonable and in good agreement with the analytic results.

We have further obtained the geometry of the current sheet deduced by the method. The deduced curvature and torsion of the MFLs in the Harris current sheet are shown in Figures 4j and 4k. The magnetic curvature reaches a maximum at the center of current sheet, which indicates that the MFLs of the Harris current sheet bend most at the center. The torsion of the magnetic field line stays almost at zero, implying the MFLs in the Harris current sheet is planar (this agrees with the theoretical calculations in Appendix D). The order of the absolute error in the torsion is very small and less than $10^{-11} R_E^{-1}$. This check is a very good validation of the new method.

After completing the above steps, iterative operation and error analysis are necessary and we will discuss these later.

4.2. Two-Dimensional Force-Free Flux Ropes

In this subsection, we attempt to investigate the complete geometry of magnetic field lines for a classic force-free flux rope model. In this model, the three components of the magnetic vector in cylindrical coordinates can be expressed (Lundquist, 1950) as:

$$B_r = 0, B_\phi = B_0 J_1(\alpha r), B_z = B_0 J_0(\alpha r), \quad (65)$$

where r is the distance from the central axis, α^{-1} is the characteristic scale of the flux rope, and J is the Bessel function. In this test, we adopt $B_0 = 60nT$ and $\alpha = 1 / R_E$. Then the characteristic scale of the flux rope is $D = 1 / \alpha = 1R_E$. The trajectory of the 4 SCs with a separation of $L = 100$ km is set to be from $(-2, 0, 0) R_E$ to $(2, 0, 0) R_E$ during 100 s (indicating the actual structure velocity is 257 km/s [0.0404 Re/s]), which is shown in Figure 5a. The average magnetic field measured by four S/C is illustrated in Figure 5b, the bipolar signature of B_y and the enhancement of B_z around the flux rope's center is apparent.

By repeating the same procedures as in Section 4.1, the quadratic magnetic gradient can be readily acquired (Figures 5c–5g). One can find that the results derived by the method are in good agreement with the analytic results obtained in Appendix E. The variations of curvature and torsion of the MFLs confirm that the magnetic topological structure is different from those of the current sheet (Figures 5h and 5i). It can also be seen from Figures 5h and 5i that the curvature of the MFLs contains a minimum, and the torsion of the MFLs contains a maximum, at the center. This indicates that the straighter and more twisted the MFLs, the nearer to the center of flux rope, implying the nonplanar and helical structure of the flux rope. This test shows that the results obtained by the approach are in good agreement with the analytical results, indicating that the estimators obtained in Sections 2 and 3 are reliable and applicable.

Figure 4. The comparison between the properties of 1-D Harris current sheet deduced from the estimators and those from the analytic calculations based on Appendix D. Panel (a) shows the current sheet configuration and the S/C trajectory in the current sheet reference frame; Panels (b) and (c) show the variation of magnetic field and current density, respectively; Panel (d) is the time series of the gradient of magnetic field; Panel (e) denotes the relative velocity of S/Cs to the current sheet; Panel (f) represents the quadratic gradient of magnetic field; Panels (g–i) denote the time series of the quadratic gradient of unit magnetic vector b_x , b_y , b_z , respectively. The magnetic field line curvature and torsion are displayed in Panel (j) and (k), respectively. The vertical black dashed line in each panel represents the center of current sheet. The solid lines in each panel are the accurate or theoretical results. The circles are the results obtained by the new method.

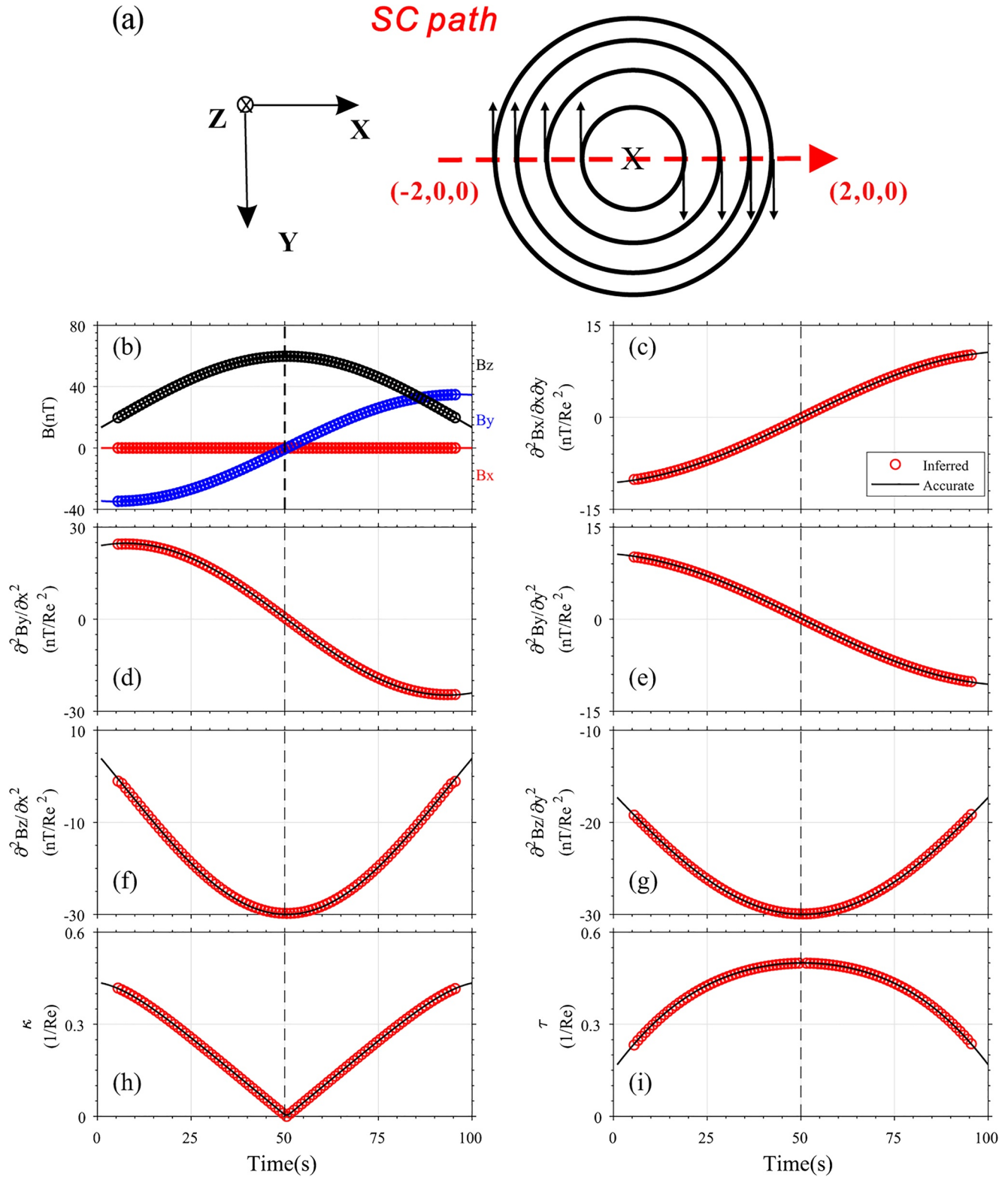


Figure 5. The properties of magnetic field lines (MFLs) of 2-D flux rope. The relative path of S/Cs to the magnetic structure is sketched in Panel (a). Panel (b) shows the variation of the magnetic field; Panels (c–g) denote the time series of the quadratic gradient of magnetic field. The magnetic field line curvature and torsion are displayed in Panels (h) and (i). The vertical black dashed line in each panel represents the center of flux rope. The circles and solid lines represent the results inferred by our method and the accurate results, respectively.

4.3. Errors

The errors of the estimators put forward in this study may arise from two types of sources: the underlying measurement errors and the truncation errors. The key measurement errors include the error in the measured magnetic field \mathbf{B} and that of the current density \mathbf{j} derived from the plasma moment data (which will be seen in the application in Section 5). The truncation errors arise from terms beyond the differential order considered here and represent neglected behavior of the magnetic structure and plasmas.

The spatial truncation errors can be approximately measured by L/D , where D is the typical spatial size of magnetic structure and L is the size of tetrahedron of four SC. When L/D is very small, the truncation errors are generally small. However, as L/D grows large, the truncation errors may become significant. The iterative operation allows us to attempt to get more accurate and reliable results.

Figure 6 compares the results of the calculations made with no iteration; with the first and second iterations, and theoretical calculation with $L/D = 0.3$. It can be seen that the iterations yield more accurate results. However, the second iteration in these examples did not produce better results than the first iteration.

Figure 7 displays the variations of the relative errors of the results with L/D . The relative error is defined as $\left| \frac{X_{method} - X_{real}}{X_{real}} \right|$, where X_{method} represents the results obtained with our method and X_{real} denotes the analytical results from the model. It is seen from Figures 7a–7e that the relative errors of the linear magnetic gradient, apparent velocity and curvature of the MFLs are of first order in L/D for no iteration calculations, but they are of second order in L/D after the first and second iterations. Nevertheless, the relative errors of the components of the quadratic magnetic gradient and the torsion of MFLs are all of first order in L/D (Figures 7f–7j), although after the first or second iterations they are improved.

Through the above analysis, one can conclude that the most accurate results are those derived by at least one iteration, especially when L/D is larger than 0.5. Thus, it is necessary to perform the first iteration when L/D is larger than 0.5.

In addition, we have performed a calculation on the modeled geomagnetosphere with no symmetry and presented the obtained results in the supplementary information, where the structure of the cusp regions has been demonstrated reasonably as in Figure S1 and S2.

5. Application: Magnetic Flux Rope

In this section, we have applied the approach developed in Sections 2 and 3 to investigate the magnetic structure and geometry of a magnetic flux rope at magnetopause, observed by MMS during 2015-10-16 13:04:33–13:04:35, which is the second of two sequential flux ropes reported by Eastwood et al., (2016), and has been analyzed by many researchers (e.g., C. Zhang et al., 2020). Here, we have used the high-resolution magnetic field data measured by the fluxgate magnetometer, operating at 128 vectors per second in burst-mode (Burch et al., 2016; Russell et al., 2016), and the plasma data provided by FPI (fast plasma investigation, measuring electrons at cadence of 30 ms and ions at cadence of 150 ms) (Pollock et al., 2016; Torbert et al., 2015). To calculate the quadratic magnetic gradient, the plasma moments are interpolated to obtain a 1/128 s time resolution to match that of the magnetic field data and to derive the current density. Note that the MMS constellation is often nearly a regular tetrahedron with its separation scale of $L \approx 20$ km during this time interval.

Typically, there are many waves affecting the magnetic field at various frequencies in space plasmas. If we calculated the time variation rates of the magnetic field and the linear and quadratic magnetic gradients directly, the errors caused by these waves would be so large that we would miss the underlying global features of the magnetic structure. To get rid of the influence of the waves, the magnetic field (Figure 8a) and current density (Figures 8b–8d) data have been filtered by a low-pass filter to eliminate disturbances with frequencies higher than 1 Hz from the data. In order to apply the method in Appendix A to calculate the temporal and spatial gradients of the magnetic field and current density, we have adopted $n = 10$ time points on each spacecraft to form a set of data. Thus, there are in total $N = 4n = 40$ points in a group of data. With

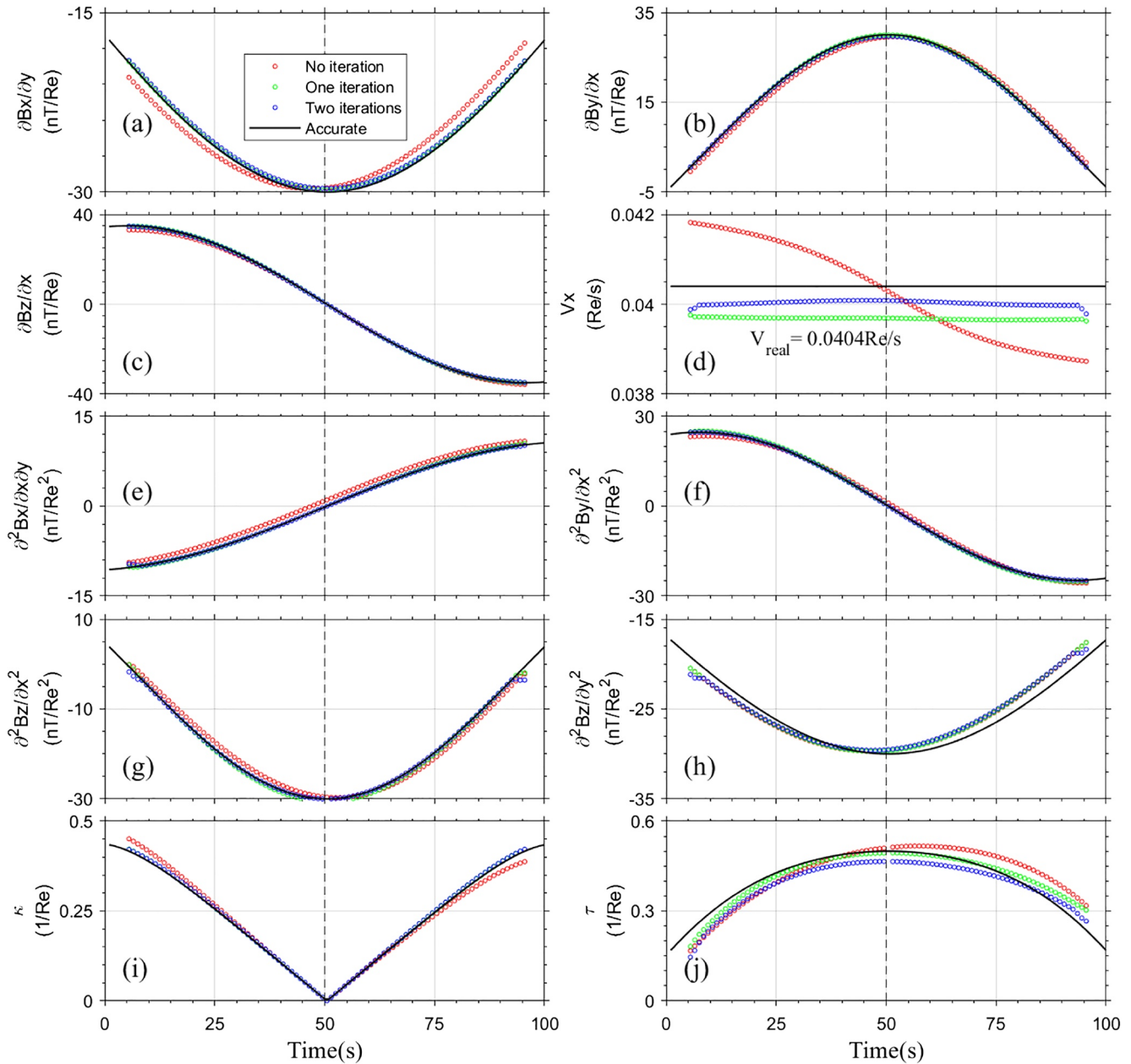


Figure 6. The comparison of those results with no iteration, first iteration and second iteration. Panel (a), (b), (c) are the time series of the linear gradients of magnetic field; Panel (d) denotes the relative velocity of S/Cs to the current sheet; Panel (e), (f), (g), (h) denote the time series of the quadratic gradients of magnetic vector, respectively. The magnetic field line curvature and torsion are displayed in Panel (i), (j), respectively. The vertical black dashed line in each panel represents the center of current sheet. The red circles in each panel denote the result of no iteration, while the green and blue circles mark the result from the first iteration and second iteration, respectively. The black solid lines represent analytic results.

this approach, the calculated temporal and spatial gradients of the magnetic field and current density have rather high accuracy.

We have derived the magnetic rotation features of the flux rope by using the MRA method illustrated in Appendix B (Shen et al., 2007). Figure 8e shows the time series of the magnetic minimum rotation direction $\hat{\mathbf{X}}_3$, which is approximately stable and nearly parallel to GSE + Y direction. Assuming the flux rope is cylindrically symmetric, $\hat{\mathbf{X}}_3$ could be approximately regarded as the orientation $\hat{\mathbf{n}}$ of the flux rope axis, that is, $\hat{\mathbf{n}} = \hat{\mathbf{X}}_3$. The helical angle of the MFLs can be defined as $\beta = a \sin(\hat{\mathbf{b}} \cdot \hat{\mathbf{n}})$. As shown in Figure 8f, the

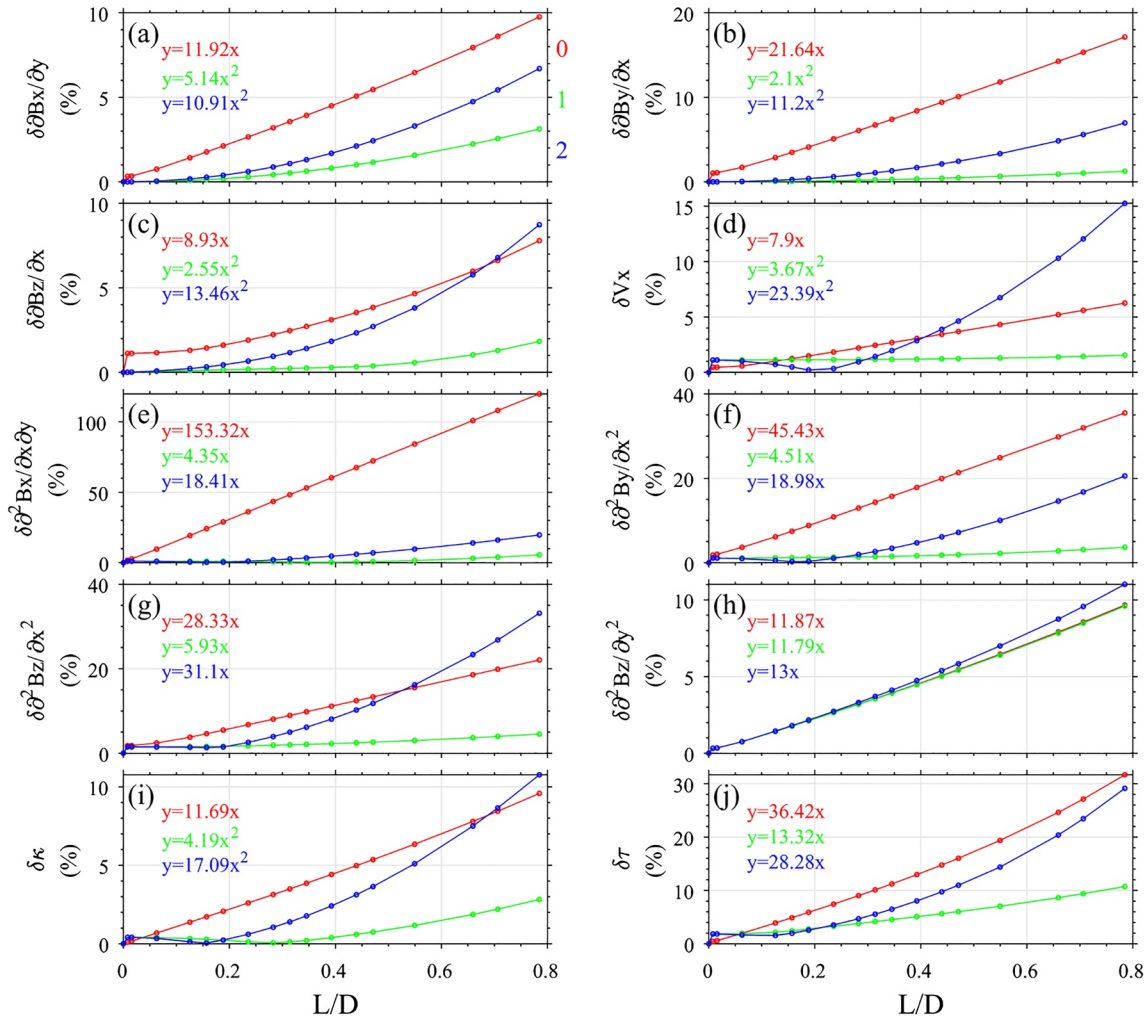


Figure 7. The relative errors (y) of the various calculated parameters of the flux rope for different L/D (x). The red solid lines in each panel are the calculation results with no iteration, while the green, blue lines represent the calculation results with the first and second iterations, respectively.

helical angle β reaches its maximum value ($\sim 89^\circ$) at the time ~ 34.1 s, implying that the MFLs lie basically along the axis orientation in the central part of the flux rope. The apparent velocity of the flux rope can be calculated by Equation 17, and is illustrated in Figure 8g. One can find that, the apparent velocity at the leading edge of flux rope is larger than that at the trailing edge, suggesting that the flux rope is decelerating and not stable during this interval. Assuming that the flux rope is steady and has a force-free magnetic field, Eastwood et al., (2016) have derived the parameters of this flux rope, and estimate that the velocity is $[-206.976, -19.8, -162.88]$ km/s in GSE, as derived by timing analysis, the axis orientation is $[-0.012, 0.989, -0.149]$ in GSE and the radius is ~ 550 km. From our analysis, it is shown that the mean velocity is $\sim [-141.408, -47.58, -96]$ km/s and the axis orientation is $[-0.0889, 0.9367, -0.3386]$ in GSE during the interval (13:04:33.5–13:04:35), when the flux rope is nearly steady. Considering the complicated motion and structure of flux rope and the different data processing approaches applied, the small discrepancy among the results is not surprising.

By using the estimators in Sections 2 and 3, the magnetic gradients and geometry of the flux rope can be obtained and these are demonstrated in Figure 9. The total 27 components of the quadratic gradient of magnetic field have been obtained with the estimators in Section 2, which are illustrated in panels (a–i) of Figure 9. It can be found that the order of the quadratic gradient of the magnetic field is generally less than 10^{-2} nT/km², while that of the first-order magnetic gradient is $\sim 10^{-1}$ nT/km. The complete geometry of the

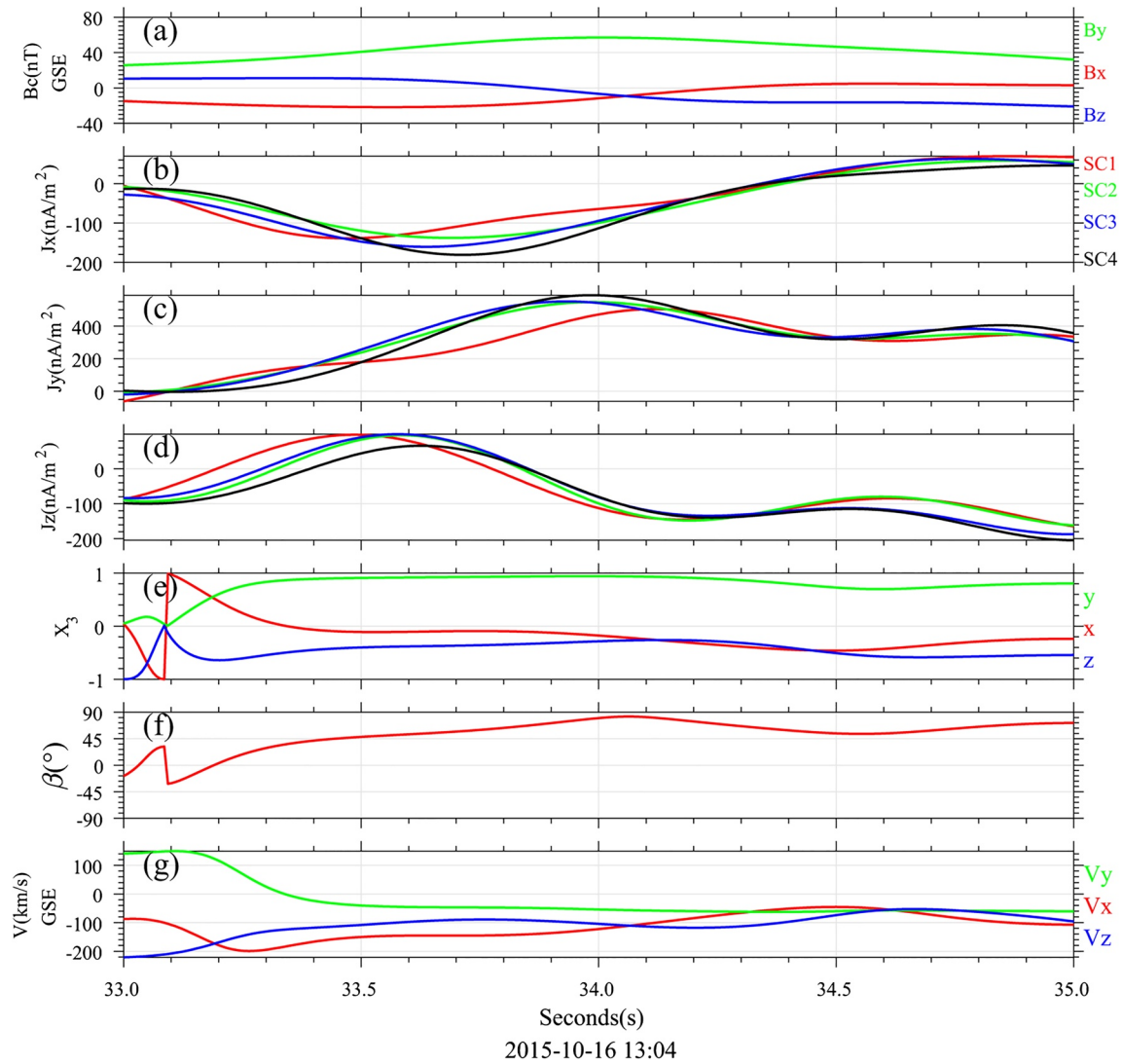


Figure 8. The parameters of the flux rope observed by MMS3 on October 16, 2015. Panel (a) shows the magnetic field at the barycenter of tetrahedron; Panels (b–d) display the components of the current density at the four S/C derived by plasma data; Panel (e) denotes the minimum rotation direction of the magnetic field lines (MFLs), which is approximately the axis direction of the flux rope; Panel (f) represents the variation of the helical angle; Panel (g) shows the apparent velocity of the flux rope relative to the magnetospheric multiscale (MMS) constellation.

MFLs in the flux rope can be derived by the estimators in Section 3, which is illustrated in Figures 9j–9l. It can be seen that the curvature of MFLs reaches its minimum value of $\sim 0.80 \times 10^{-3}/\text{km}$ (Figure 9j) and the torsion reaches its maximum value of $\sim 0.012/\text{km}^2$ (Figure 9l) at ~ 34.1 s, when the helical angle is the largest (Figure 8f). These features indicate that this flux rope is a typical one and is consistent with the 2-D flux rope model in Appendix E. The maximum curvature of the MFLs is about $\sim 3.0 \times 10^{-3}/\text{km}$, while accordingly the minimum radius of the curvature of the MFLs is ~ 330 km. We can choose this as the characteristic scale of the flux rope, that is, $D = 330$ km. Furthermore, assuming the flux rope has a cylindrical helical structure, the torsion of MFLs can also be obtained directly from the curvature and helical angle from Equation E9 in Appendix E. From Figure 9l, it can be seen that the results obtained by both techniques show good agreement with each other. Obviously, the magnetic field lines in this flux rope are right-hand spirals generally. These results verify the effectiveness and applicability of the estimators given in Sections 2 and 3. Since $L/D \approx 20/330 \approx 0.06$, we do not need to perform the iteration in this case because the accuracy of the linear results with no iteration is already very high.

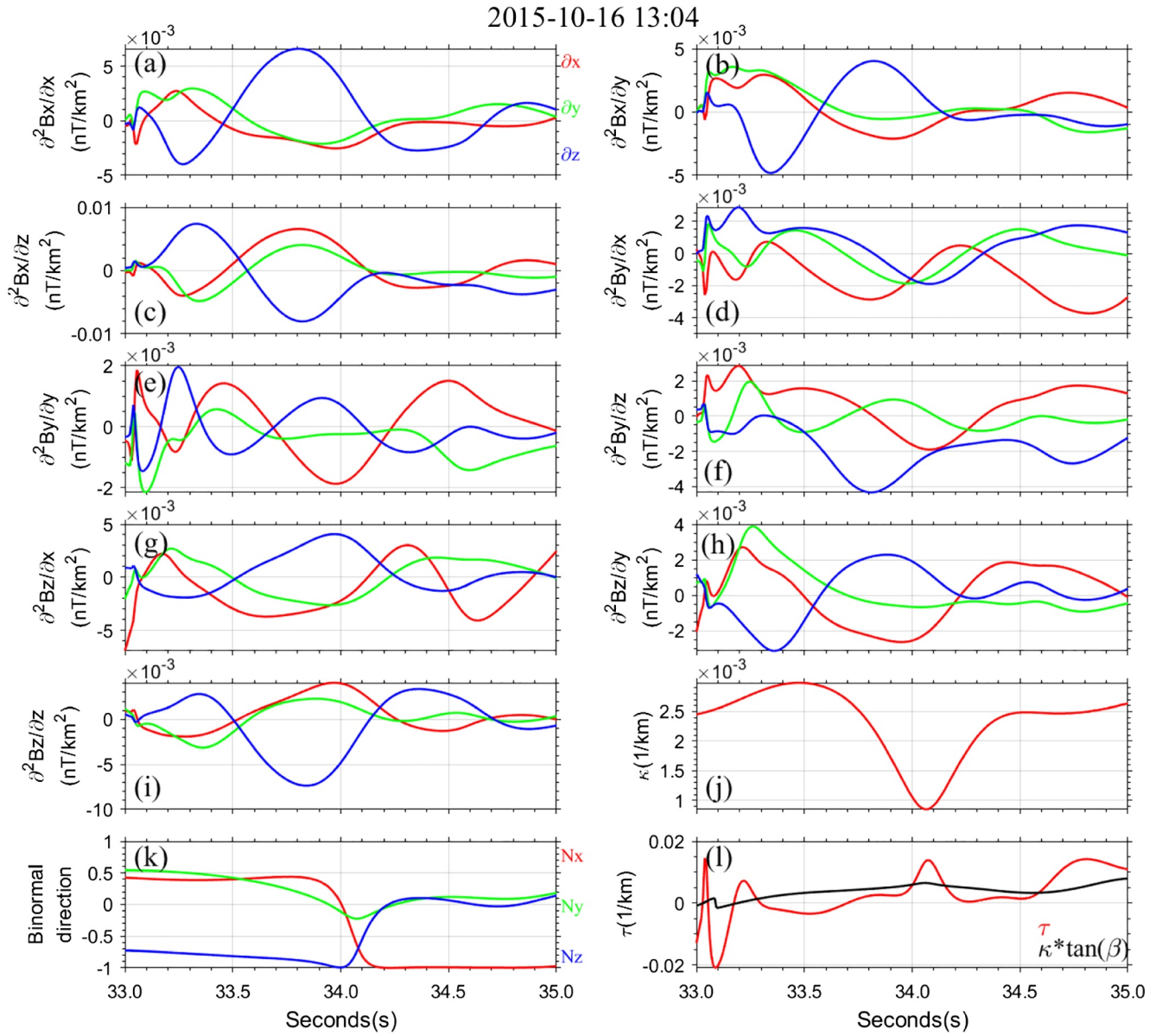


Figure 9. The magnetic structure of the flux rope on October 16, 2015. Panel (a–i) show all the 27 components of the quadratic gradient of magnetic field, where the red, green and blue lines represent the partial derivative ∂x , ∂y , ∂z , respectively; Panel (j) gives the time series of the curvature of the magnetic field lines (MFLs); Panel (k) represents the binormal direction of the MFLs; Panel (l) shows the torsion of the MFLs, with its value calculated by the magnetic gradients represented by the red line, and that drawn from the cylindrical symmetry approximation denoted by the black line.

6. Summary and Discussions

The quadratic magnetic gradient is a key parameter of the magnetic field, with which the fine structure of a magnetic structure can be revealed, as well as the twisting property of the magnetic field. However, up to now, the quadratic magnetic gradient from multi-S/C constellation measurements has not been explicitly calculated. Chanteur (1998) showed that in order to get the quadratic magnetic gradient from multipoint magnetic observations, in general, the number of S/C in the constellation has to be equal to or larger than 10, which is difficult to realize in present space exploration. Fortunately, the MMS constellation can not only provide rather accurate four-point magnetic field, but can also produce very good four-point current density estimates from particle measurements, such as to allow the quadratic magnetic gradient problem to be solved in the manner discussed here.

This paper provides a method to obtain the linear and quadratic magnetic gradients as well as the apparent velocity of the magnetic structure, based on the four-point magnetic field and current density observations and give their explicit estimators. Furthermore, the complete geometry of the magnetic field lines is revealed on the bases of these linear and quadratic magnetic gradients, and the estimator for the torsion of the MFLs is given. Simple, but relevant, tests on this novel algorithm have been made for a Harris current sheet and a force-free flux rope model, and the effectiveness and accuracy of these estimators have been verified.

In this approach (NMG algorithm), the physical quantities to be determined are as follows: the magnetic field \mathbf{B}_c (three parameters); the linear magnetic gradient $(\nabla\mathbf{B})_c$ (nine parameters); quadratic magnetic gradient $(\nabla\nabla\mathbf{B})_c$ ($6 \times 3 = 18$ parameters), and the apparent velocity of the magnetic structure \mathbf{V} (three parameters); resulting in a total of $3 + 9 + 18 + 3 = 33$ undetermined parameters.

On the other hand, the input conditions for this algorithm are: the time series of magnetic field $\mathbf{B}_a(t)$ at four points ($3 \times 4 = 12$ parameters); the transformation relationships $\frac{\partial\mathbf{B}}{\partial t} = -\mathbf{V} \cdot \nabla\mathbf{B}$ (three independent constraint equations) and $\frac{\partial}{\partial t}\nabla\mathbf{B} = -\mathbf{V} \cdot \nabla\nabla\mathbf{B}$ ($3 \times 3 = 9$ independent constraint equations); the formula $\nabla(\nabla \times \mathbf{B}) = \nabla\mathbf{j}$, derived from Ampere's law ($2 \times 3 - 1 = 5$ independent constraints); the equation $\nabla(\nabla \cdot \mathbf{B}) = 0$, from the solenoidal condition of the magnetic field ($3 - 1 = 2$ independent constraints), and finally the constraint equations $\frac{\partial}{\partial X_3} \frac{\partial}{\partial X_3} b_p = 0$, as deduced from MRA (two independent constraints); resulting in a total of $12 + 3 + 9 + 5 + 2 + 2 = 33$ independent parameters or constraints.

We note that the contribution of the current density measurements in this approach is the first order gradient of the current density, which is related to the quadratic magnetic gradient by Ampere's law. Considering the conservation of the current density $\nabla \cdot \mathbf{j} = 0$ and $\partial_3 \nabla\mathbf{B}$ already obtained from the constraint equation $\frac{\partial}{\partial t}\nabla\mathbf{B} = -\mathbf{V} \cdot \nabla\nabla\mathbf{B}$, the constraint equation $\nabla(\nabla \times \mathbf{B}) = \nabla\mathbf{j}$ yields only $2 \times 3 - 1 = 5$ independent constraints ($\partial_3(\nabla \times \mathbf{B}) = \partial_3\mathbf{j}$ is not independent). Similarly, $\nabla(\nabla \cdot \mathbf{B}) = 0$ provides only $3 - 1 = 2$ independent constraints.

Therefore, the linear and quadratic magnetic gradients, and the apparent velocity of the magnetic structure, can be completely determined based on the four-point magnetic field and current density measured by the MMS constellation.

The calculations have been expressed as being carried out in the S/C constellation frame. The NMG algorithm proceeds as follows. First, under the linear approximation, the temporal and spatial gradients of the magnetic field $(\nabla\mathbf{B}, \frac{\partial\mathbf{B}}{\partial t})$ and of the current density $(\nabla\mathbf{J}, \frac{\partial\mathbf{J}}{\partial t})$ at the barycenter of the S/C constellation can be obtained by the least squares gradient calculations as demonstrated in Appendix A. The time rate of change of the linear magnetic gradient, $\frac{\partial}{\partial t}(\nabla\mathbf{B})_c$, and the second order time derivative of the magnetic field can also be obtained. The apparent velocity of the magnetic structure relative to the S/C frame system can then be readily obtained with the formula $\frac{\partial\mathbf{B}}{\partial t} = -\mathbf{V} \cdot \nabla\mathbf{B}$, and also the gradient of the linear magnetic gradient along the direction of motion, $(\nabla_3\nabla\mathbf{B})_c$. With the constraint equation $\nabla(\nabla \times \mathbf{B}) = \nabla\mathbf{j}$, the transverse quadratic magnetic gradient of the longitudinal magnetic field B_3 , $\nabla_p \nabla_q B_3$ ($p, q = 1, 2$), can be found. Finally, the transverse quadratic magnetic gradients of the transverse magnetic field, $\partial_p \partial_q B_s$ (t, r_c), can be obtained by using the constraint equations $\nabla(\nabla \cdot \mathbf{B}) = 0$, $\nabla(\nabla \times \mathbf{B}) = \nabla\mathbf{j}$, and magnetic rotation feature $\frac{\partial}{\partial X_3} \frac{\partial}{\partial X_3} b_p = 0$. Therefore, all the 18 independent components of the quadratic magnetic gradient can be calculated.

The quadratic magnetic gradient, obtained with no iteration, has a truncation error of the first order in L/D because the linear approximation has been made. To find a more accurate quadratic magnetic gradient, an iterative procedure can be performed. In this procedure, the magnetic field, the linear magnetic gradient, and the time derivative of the linear magnetic gradient are corrected by using the quadratic magnetic gradient calculated initially and the above steps are then repeated, so as to achieve the components of the

corrected quadratic magnetic gradient. After this first iteration, the magnetic field, linear magnetic gradient, the apparent velocity of the magnetic structure at the barycenter of the S/C tetrahedron all have their accuracies improved significantly and have truncation errors in the second order of L/D , while the accuracy of the quadratic magnetic gradient obtained is also enhanced.

This algorithm is valid for both stationary and nonstationary structures, whether the magnetic structures are moving at a constant velocities or accelerating/decelerating. It is noted that the magnetic field, linear and quadratic magnetic gradients are identical for different inertial frames of reference.

With the magnetic field, linear and quadratic magnetic gradients found, the complete geometry of the MFLs can be determined, including the natural coordinates or Frenet coordinates (tangential unit vector, principal normal and binormal), curvature, and torsion. The corresponding estimators for the geometrical features have been given.

The algorithm for estimating the quadratic magnetic gradient and the geometry of the MFLs have been demonstrated with the Harris current sheet and cylindrical flux rope, and its correctness has been verified. It is found that, the errors of the linear quadratic magnetic gradients, apparent velocity of the magnetic structure, and the geometrical parameters are of first order in L/D when no iteration is made. If one iteration is performed, the accuracies of the linear magnetic gradient, apparent velocity of the magnetic structure, curvature of the MFLs are improved significantly and their errors appear at the second order in L/D , while the accuracies of the quadratic magnetic gradient and the torsion of the MFLs are also enhanced. To determine the first order magnetic gradient and apparent relative velocity of the magnetic structure, this algorithm is more accurate than the previous approaches based on the linearity approximation (Chan-teur, 1998; Harvey, 1998; Shi et al., 2006).

We have also applied the algorithm developed in this research to investigate the magnetic structure of one flux rope measured by MMS (Eastwood et al., 2016), showing good results. The applicability of this approach is therefore verified.

If the magnetic gradients with orders higher than two are neglected the magnetic field can be expressed as

$$\mathbf{B}(t, \mathbf{r}) = \mathbf{B}(t, \mathbf{r}_c) + (\mathbf{r} - \mathbf{r}_c) \cdot \nabla \mathbf{B}(t, \mathbf{r}_c) + \frac{1}{2} (\mathbf{r} - \mathbf{r}_c)(\mathbf{r} - \mathbf{r}_c) \cdot \nabla \nabla \mathbf{B}(t, \mathbf{r}_c). \quad (65a)$$

with the MMS magnetic field and current density measurements, the linear and quadratic magnetic gradients at the barycenter are obtained, such that the local spatial distribution of the magnetic field, as well as the MFLs, can be obtained.

Appendix A: The Explicit Estimators for the Linear Gradients of Field in Space and Time

De Keyser et al. (2007) has put forward an algorithm for calculating the gradients in space and time of a field, which they called Least-Squares Gradient Calculation (LSGC). Here we will find the explicit estimator of the four-dimensional linear gradients of a scalar field or one component of the vector field with corrections from the quadratic gradients.

Considering the 4 S/C of the constellation obtained time series of measurements on a certain physical quantity investigated, as illustrated in Figure 1 in Section 2. Here the S/C constellation reference frame is used. Assuming each S/C makes observations at n times, in total $N = 4n$ measurements are made by the constellation, which form a set of data. In the previous work of De Keyser, et al. (2007), it is supposed that, in this area of spacetime, the physical quantity concerned is approximately varying linearly, and the linear gradients of field in space and time are about homogeneous. Here, however, the homogeneity assumption is not necessary because the quadratic gradients have been included. In the S/C constellation coordinate system, the position of the observation point is $x_{(a)}^{\mu} = (x_a, y_a, z_a, t_a)$ ($\mu = 1, 2, 3, 4$). It is convenient to use the dimensionless length and time in the investigation. If the characteristic size of the S/C constellation is L and the time resolution of the observations is T , we can make the transformation: $x_a / L \rightarrow x_a, t_a / T \rightarrow t_a$.

Obviously, in the S/C constellation reference frame, the four S/C are nearly motionless and their space coordinates $x_{(a)}^i = (x_a, y_a, z_a)$ do not change with time during typical structure crossing events.

In the S/C constellation reference frame, at the space time $x_{(a)}^\mu = (x_a, y_a, z_a, t_a)$ ($\mu = 1, 2, 3, 4$), the physical quantity measured is $f(x_{(a)}^\mu) = f_{(a)}$, its gradients are $\frac{\partial f}{\partial x^\mu} = \nabla_\mu f \equiv \left(\frac{\partial f}{\partial x}, \frac{\partial f}{\partial y}, \frac{\partial f}{\partial z}, \frac{\partial f}{\partial t} \right)$. The spacetime coordinates at the central point satisfy

$$\sum_{a=1}^N \Delta x_{(a)}^\mu = \sum_{a=1}^N (x_{(a)}^\mu - x_c^\mu) = 0. \quad (\text{A1})$$

Thus the spacetime coordinates at the central point are

$$x_c^\mu = \frac{1}{N} \sum_{a=1}^N x_{(a)}^\mu. \quad (\text{A2})$$

Here x_c^i are the space coordinates of the barycenter of the S/C constellation, which have fixed values and can be chosen as $x_c^i = 0$. $x_c^4 = t_c$ is the average time of the $4n$ observations.

The physical quantity $f_{(a)}$ measured at the point $x_{(a)}^\mu$ can be expanded around the central point x_c^μ as (The second Taylor series)

$$f_{(a)} = f_c + \Delta x_{(a)}^\nu \nabla_\nu f_c + \frac{1}{2} \Delta x_{(a)}^\nu \Delta x_{(a)}^\lambda \nabla_\nu \nabla_\lambda f_c \quad (\text{A3})$$

Or

$$f_{(a)} = f_c + \Delta x_{(a)}^\nu G_\nu + \frac{1}{2} \Delta x_{(a)}^\nu \Delta x_{(a)}^\lambda G_{\nu\lambda} \quad (\text{A3a})$$

Here, the first order gradient $G_\nu = (\nabla_\nu f)_c$, and the quadratic gradient $G_{\nu\lambda} = (\nabla_\nu \nabla_\lambda f)_c$. There are five parameters ($f_c, G_\nu = (\nabla_\nu f)_c$) to be determined.

Construct the action

$$S = \frac{1}{N} \sum_a \left[f_c + \Delta x_{(a)}^\nu G_\nu + \frac{1}{2} \Delta x_{(a)}^\nu \Delta x_{(a)}^\lambda G_{\nu\lambda} - f_{(a)} \right]^2 \quad (\text{A4})$$

To minimize it, let

$$\delta S = 0. \quad (\text{A5})$$

Such as to obtain f_c and $G_\nu = \nabla_\nu f_c$ at the central point. The above equation leads to

$$\frac{\partial S}{\partial f_c} = 0, \frac{\partial S}{\partial G_\nu} = 0, \frac{\partial S}{\partial G_{\nu\lambda}} = 0. \quad (\text{A6})$$

Since

$$\begin{aligned} \frac{\partial S}{\partial f_c} &= \frac{1}{N} \sum_{a=1}^N 2 \left[f_c + \Delta x_{(a)}^\nu G_\nu + \frac{1}{2} \Delta x_{(a)}^\nu \Delta x_{(a)}^\lambda G_{\nu\lambda} - f_{(a)} \right] \\ &= 2 \cdot \frac{1}{N} \sum_{a=1}^N \left[f_c - f_{(a)} \right] + 2 \cdot \frac{1}{N} \sum_{a=1}^N \Delta x_{(a)}^\nu G_\nu + \frac{1}{N} \sum_{a=1}^N \Delta x_{(a)}^\nu \Delta x_{(a)}^\lambda G_{\nu\lambda} = 0. \end{aligned} \quad (\text{A7})$$

Considering Equation A1, it reduces to

$$f_c = \frac{1}{N} \sum_a f_{(a)} - \frac{1}{2N} \sum_a \Delta x_{(a)}^\nu \Delta x_{(a)}^\lambda G_{\nu\lambda}. \quad (\text{A8})$$

or

$$f_c = \frac{1}{N} \sum_a f_{(a)} - \frac{1}{2} R^{\nu\lambda} G_{\nu\lambda}. \quad (\text{A8a})$$

where the general volume tensor $R^{\mu\nu}$ is defined as

$$R^{\mu\nu} \equiv \frac{1}{N} \sum_{a=1}^N \Delta x_{(a)}^\mu \Delta x_{(a)}^\nu = \frac{1}{N} \sum_{a=1}^N \left(x_{(a)}^\mu - x_c^\mu \right) \left(x_{(a)}^\nu - x_c^\nu \right). \quad (\text{A9})$$

Equation A8a gives the value of physical quantity f at the barycenter of the constellation with corrections by the quadratic gradients.

Furthermore,

$$\begin{aligned} 0 &= \frac{\delta S}{\delta G_\mu} = \frac{1}{N} \sum_{a=1}^N 2 \left[f_c - f_{(a)} + \Delta x_{(a)}^\nu G_\nu + \frac{1}{2} \Delta x_{(a)}^\nu \Delta x_{(a)}^\lambda G_{\nu\lambda} \right] \nabla x_{(a)}^\mu \\ &= -2 \cdot \frac{1}{N} \sum_{a=1}^N f_{(a)} \Delta x_{(a)}^\mu + 2 R^{\mu\nu} G_\nu + R^{\mu\nu\lambda} G_{\nu\lambda}, \end{aligned} \quad (\text{A10})$$

where the 3 order tensor $R^{\mu\nu\lambda}$ is defined as

$$R^{\mu\nu\lambda} \equiv \frac{1}{N} \sum_{a=1}^N \Delta x_{(a)}^\mu \Delta x_{(a)}^\nu \Delta x_{(a)}^\lambda. \quad (\text{A11})$$

From Equation A10 we get

$$R^{\mu\nu} G_\nu = \frac{1}{N} \sum_{a=1}^N \left(x_{(a)}^\mu - x_c^\mu \right) f_a - \frac{1}{2} R^{\mu\nu\lambda} G_{\nu\lambda}. \quad (\text{A12})$$

Thus the linear gradients at the central point are

$$G_\nu = \left(\nabla_\nu f \right)_c = \left(R^{-1} \right)_{\nu\mu} \cdot \frac{1}{N} \sum_{a=1}^N \left(x_{(a)}^\mu - x_c^\mu \right) f_a - \frac{1}{2} \left(R^{-1} \right)_{\nu\mu} R^{\mu\sigma\lambda} G_{\sigma\lambda}. \quad (\text{A13})$$

Here R^{-1} satisfies $\left(R^{-1} \right)_{\nu\sigma} R^{\sigma\lambda} = R^{\lambda\sigma} \left(R^{-1} \right)_{\sigma\nu} = \delta_\nu^\lambda$. These are the first order gradients of the physical quantity in space and time at the central point with corrections by the quadratic gradients.

Under the linear approximation, the quadratic gradient is neglected, that is, $G_{\nu\lambda} = 0$. From Equation A8a, the physical quantity at the central point is

$$f_0 = \frac{1}{N} \sum_{a=1}^N f_{(a)}. \quad (\text{A14})$$

From Equation A13, the first order gradients of the physical quantity in space and time are

$$G_\nu = \left(\nabla_\nu f \right)_c = \left(R^{-1} \right)_{\nu\mu} \cdot \frac{1}{N} \sum_{a=1}^N \left(x_{(a)}^\mu - x_c^\mu \right) f_a. \quad (\text{A15})$$

Appendix B: Nature of the Magnetic Rotation Tensor

In previous investigations (Shen et al., 2007; Shen, Liu, et al., 2008; Shen, Rong, et al., 2008), the MRA (magnetic rotation analysis) method has been put forward to study the three-dimensional rotational properties of the magnetic field. We may construct the magnetic rotational tensor \mathbf{S} based on the gradient of the magnetic unit vector $\hat{\mathbf{b}}$, which is defined as $S_{ij} \equiv \nabla_i b_l \nabla_j b_l$. Because the tensor \mathbf{S} is symmetrical ($S_{ij} = S_{ji}$, $i, j = 1, 2, 3$), it has three eigenvectors, $\hat{\mathbf{X}}_1$, $\hat{\mathbf{X}}_2$ and $\hat{\mathbf{X}}_3$, and three corresponding eigenvalues, μ_1 , μ_2 and μ_3 with $\mu_1 \geq \mu_2 \geq \mu_3 \geq 0$. Actually, the third eigenvalue μ_3 is zero. Fadanelli et al. (2019) has presented one verification on this property of the magnetic rotational tensor. To facilitate the understanding, here we can show another verification as the following.

The length of $\hat{\mathbf{b}}$ is 1, and $\hat{\mathbf{b}} \cdot \hat{\mathbf{b}} = 1$, so that

$$\nabla_i \left(\hat{\mathbf{b}} \cdot \hat{\mathbf{b}} \right) = \left(\nabla_i b_j \right) b_j = 0. \quad (\text{B1})$$

To ensure the existence of $\hat{\mathbf{b}}$, it is necessary that

$$\text{Det}(\nabla_i b_j) = 0. \quad (\text{B2})$$

Based on its definition, the determinant of the magnetic rotation tensor is

$$\text{Det}(S_{ij}) = \text{Det}(\nabla_i b_l) \cdot \text{Det}(\nabla_j b_l) = 0. \quad (\text{B3})$$

On the other hand,

$$\text{Det}(S_{ij}) = \mu_1 \mu_2 \mu_3, \mu_1 \geq \mu_2 \geq \mu_3 \geq 0. \quad (\text{B4})$$

Thus Equations A3 and A4 reduce to

$$\mu_3 = 0. \quad (\text{B5})$$

So that the third eigenvalue μ_3 of the magnetic rotation tensor $S_{ij} = \nabla_i b_l \nabla_j b_l$ is null definitely.

Appendix C: Another Verification on the Formula of Torsion of MFLs in Terms of Magnetic Gradients

Based on the definition, the torsion of the MFLs

$$\begin{aligned} \tau &= \frac{1}{\kappa} \frac{d\kappa}{ds} \cdot \hat{\mathbf{N}} \\ &= \frac{1}{\kappa} \frac{d}{ds} \left(\frac{d\mathbf{B}}{ds} \right) \cdot \hat{\mathbf{N}}. \\ &= \frac{1}{\kappa} \left(\frac{1}{B} \frac{d^2 \mathbf{B}}{ds^2} + 2 \frac{d}{ds} \frac{1}{B} \cdot \frac{d\mathbf{B}}{ds} + \mathbf{B} \frac{d^2}{ds^2} \frac{1}{B} \right) \cdot \hat{\mathbf{N}} \end{aligned} \quad (\text{C1})$$

Due to $\mathbf{B} \cdot \hat{\mathbf{N}} = 0$, $\frac{d\mathbf{B}}{ds} \cdot \hat{\mathbf{N}} = \left(B \frac{d\hat{\mathbf{b}}}{ds} + \frac{dB}{ds} \hat{\mathbf{b}} \right) \cdot \hat{\mathbf{N}} = \left(B\kappa + \frac{dB}{ds} \hat{\mathbf{b}} \right) \cdot \hat{\mathbf{N}} = 0$, the second and third terms at the left hand of the above formula disappear. Therefore

$$\tau = \frac{1}{\kappa B} \frac{d^2 \mathbf{B}}{ds^2} \cdot \hat{\mathbf{N}}. \quad (\text{C2})$$

This gives the relationship between the torsion of the MFLs and the second order derivative of the magnetic field along the MFLs.

Furthermore, the torsion of the MFLs becomes

$$\begin{aligned} \tau &= \frac{1}{\kappa B} \hat{\mathbf{N}} \cdot \frac{d}{ds} \left(\frac{1}{B} B_i \partial_i \mathbf{B} \right) \\ &= \frac{1}{\kappa B} \hat{\mathbf{N}} \cdot \left[\left(\frac{d}{ds} \frac{1}{B} \right) B_i \partial_i \mathbf{B} + \frac{1}{B} \left(\frac{d}{ds} B_i \right) \partial_i \mathbf{B} + \frac{1}{B} B_i \frac{d}{ds} \partial_i \mathbf{B} \right]. \end{aligned} \quad (\text{C3})$$

The first term at the left hand of the above formula disappears because $\hat{\mathbf{N}} \cdot (B_i \partial_i \mathbf{B}) = B \hat{\mathbf{N}} \cdot \frac{d}{ds} \mathbf{B} = 0$ as already shown below Equation C1. So that the torsion

$$\begin{aligned} \tau &= \frac{1}{\kappa B} \hat{\mathbf{N}} \cdot \left[\frac{1}{B} \left(\frac{d}{ds} B_i \right) \partial_i \mathbf{B} + \frac{1}{B} B_i \frac{d}{ds} \partial_i \mathbf{B} \right] \\ &= \frac{1}{\kappa B^3} N_m B_n \partial_n B_i \partial_i B_m + \frac{1}{\kappa B^3} N_m B_i B_n \partial_n \partial_i B_m. \end{aligned} \quad (\text{C4})$$

Appendix D: Geometry of the MFLs in One-Dimensional Current Sheets

Here, the properties of the one-dimensional current sheets are the update to the results in Appendix D in the previous study (Shen et al., 2003). It is assumed that the magnetic field in the 1 dimensional current sheets is $\mathbf{B} = B_x \hat{\mathbf{e}}_x + B_y \hat{\mathbf{e}}_y + B_z \hat{\mathbf{e}}_z$. Let the z axis to be along the normal to the 1 dimensional current sheets.

The components of the magnetic field in the x and y directions are invariants, that is, $\partial_x = 0, \partial_y = 0$. Therefore the components of the magnetic field in the Cartesian coordinates are

$$\begin{cases} B_x = B_0 \eta(z) \\ B_y = \text{Const.} \\ B_z = \text{Const.} \end{cases} \quad (\text{D1})$$

We may choose that $B_z \geq 0, B_0 > 0, \partial_z B_x = B_0 \eta'(z) > 0$. As for the Harris current sheets (Harris, 1962), the function $\eta(z) = \tanh(z/h)$, where h is the half width of the current sheets. The total magnetic strength is $B = (B_x^2 + B_y^2 + B_z^2)^{1/2}$.

The curvature of the MFLs is

$$\begin{aligned} \kappa &= \hat{\mathbf{b}} \cdot \nabla \hat{\mathbf{b}} \\ &= B^{-2} (\mathbf{B} \cdot \nabla) \mathbf{B} - \frac{1}{2} B^{-4} (\mathbf{B} \cdot \nabla) B^2 \cdot \mathbf{B} \\ &= B^{-4} B_z \partial_z B_x \left[(B_y^2 + B_z^2) \hat{\mathbf{e}}_x - B_x B_y \hat{\mathbf{e}}_y - B_x B_z \hat{\mathbf{e}}_z \right] \end{aligned} \quad (\text{D2})$$

The value of the curvature is

$$\kappa = B^{-3} B_z (B_y^2 + B_z^2)^{1/2} \partial_z B_x. \quad (\text{D3})$$

The radius of the curvature is $R_c = 1 / \kappa$.

The principal normal vector is

$$\hat{\mathbf{K}} = \kappa / \kappa = B^{-1} (B_y^2 + B_z^2)^{1/2} \left[(B_y^2 + B_z^2) \hat{\mathbf{e}}_x - B_x B_y \hat{\mathbf{e}}_y - B_x B_z \hat{\mathbf{e}}_z \right]. \quad (\text{D4})$$

The binormal vector is

$$\hat{\mathbf{N}} = \hat{\mathbf{b}} \times \hat{\mathbf{K}} = B^{-1} \mathbf{B} \times \hat{\mathbf{K}} = (B_y^2 + B_z^2)^{1/2} (B_z \hat{\mathbf{e}}_y - B_y \hat{\mathbf{e}}_z). \quad (\text{D5})$$

Therefore, the binormal of the MFLs is constant. Then, based on the definition (58), the torsion of MFLs is

$$\tau = -\frac{1}{\kappa} \kappa \cdot \frac{d\hat{\mathbf{N}}}{ds} = 0. \quad (\text{D6})$$

So that, the MFLs in the current sheets as formulated by (D1) are plane curves. For the asymmetric current sheet, $\eta(z) = \alpha + \tanh(z/h), 1 > \alpha > 0$. As for the shock fronts, $B_y = 0$, and $\eta(z) = \alpha + \tanh(z/h), \alpha > 1$. For these cases, the MFLs are plane curves with zero torsion.

However, as shown in actual observations, the component B_y is not constant, which maximizes at the center of neutral sheets and is decreasing away from the center of the current sheets (Rong, et al., 2012). The MFLs in the magnetotail current sheets often have a shape of helix in the neutral sheets (Shen, Liu, et al., 2008).

Appendix E: Geometry of Cylindrical Helical MFLs in Magnetic Flux Ropes With Axial Symmetry

Cylindrical spiral MFLs are common in space plasmas, as seen in FTEs (Lee et al., 1985; Liu & Hu, 1988; Russell & Elphic, 1979; Y. Liu et al., 2018; Lockwood & Hapgood, 1998; Wang et al., 2007) or flux ropes caused by local magnetic reconnection processes (Kivelson et al., 1995; Pu et al., 2005; Sibeck, et al., 1984; Slavin et al., 1989; Slavin et al., 2003; Zong et al., 2004; Y. C. Zhang et al., 2007), fast tailward escaping plasmoids (Slavin et al., 1989; Slavin et al., 1995), etc.

As shown in Figure E1, polar coordinates are used. The central axis is along the z axis, the arc length is s , the distance from the central axis is r , and the azimuthal angle is ϕ . The radial unit vector is $\hat{\mathbf{e}}_r$, and the azimuthal unit vector is $\hat{\mathbf{e}}_\phi$. The tangent vector of the MFLs is

$$\hat{\mathbf{b}} = \mathbf{B} / B = \cos \beta \hat{\mathbf{e}}_\phi + \sin \beta \hat{\mathbf{e}}_z, \quad (\text{E1})$$

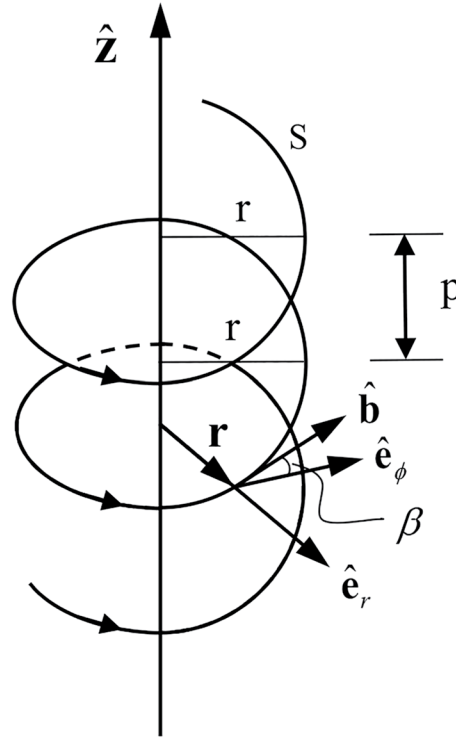


Figure E1. Demonstration on the cylindrical spiral magnetic field lines (MFLs).

where β is the helix angle of the MFLs. The helical pitch is $p = 2\pi r \tan \beta$. Define the rotation frequency $\omega \equiv d\phi / ds$. Then, $\omega = \phi / s = 2\pi / (p / \sin \beta) = \cos \beta / r$. Thus,

$$\frac{ds}{d\phi} = \frac{1}{\omega} = \frac{r}{\cos \beta}. \quad (\text{E2})$$

The curvature of the MFLs is

$$\boldsymbol{\kappa} = \frac{d\hat{\mathbf{b}}}{ds} = \frac{d\phi}{ds} \frac{d\hat{\mathbf{b}}}{d\phi} = \omega \cos \beta \frac{d\hat{\mathbf{e}}_\phi}{d\phi} = -\omega \cos \beta \hat{\mathbf{e}}_r. \quad (\text{E3})$$

where, $\frac{d}{d\phi} \hat{\mathbf{e}}_\phi = -\hat{\mathbf{e}}_r$ is used.

The value of the curvature is

$$\kappa = \omega \cos \beta = r\omega^2 = r^{-1} \cos^2 \beta. \quad (\text{E4})$$

The radius of curvature is

$$R_c = r (\cos \beta)^{-2}. \quad (\text{E5})$$

The principal vector of the helical MFLs is $\hat{\mathbf{K}} = \boldsymbol{\kappa} / \kappa = -\hat{\mathbf{e}}_r$, that is along the radial direction. The binormal $\hat{\mathbf{N}}$ is

$$\hat{\mathbf{N}} = \hat{\mathbf{b}} \times \hat{\mathbf{K}} = \cos \beta \cdot \hat{\mathbf{e}}_z - \sin \beta \cdot \hat{\mathbf{e}}_\phi. \quad (\text{E6})$$

The variation rate of the binormal $\hat{\mathbf{N}}$ along the MFLs is

$$\frac{d\hat{\mathbf{N}}}{ds} = \frac{d\phi}{ds} \cdot \frac{d\hat{\mathbf{N}}}{d\phi} = \omega (-\sin \beta) \frac{d\hat{\mathbf{e}}_\phi}{d\phi} = \omega \sin \beta \cdot \hat{\mathbf{e}}_r. \quad (\text{E7})$$

So that the torsion of the helical MFLs is

$$\tau = -\hat{\mathbf{K}} \cdot \frac{d\hat{\mathbf{N}}}{ds} = \omega \sin \beta = r^{-1} \sin \beta \cos \beta = 2\pi p^{-1} \sin^2 \beta. \quad (\text{E8})$$

On the contrary, if the curvature κ and torsion τ of the cylindrical spiral MFLs have been measured, the helix angle, the distance from the central axis, the spiral pitch and the rotation frequency can be expressed as

$$\tan \beta = \frac{\tau}{\kappa} = \tau R_c, \quad (\text{E9})$$

$$r = \kappa^{-1} \cos^2 \beta = \frac{\kappa}{\tau^2 + \kappa^2}, \quad (\text{E10})$$

$$p = 2\pi r \tan \beta = \frac{2\pi\tau}{\tau^2 + \kappa^2}, \quad (\text{E11})$$

$$\omega = \frac{\cos \beta}{r} = \sqrt{\tau^2 + \kappa^2}. \quad (\text{E12})$$

Any arbitrary magnetic field line can locally be fitted by a cylindrical spiral arc with the same curvature and torsion. The curvatures of the magnetic field lines are always nonnegative. However, the torsion of one MFL can be either positive or negative. When $\tau > 0$, the helix angle $\beta > 0$, the magnetic field line is locally a right-hand cylindrical spiral; while $\tau < 0$, $\beta < 0$, it is a left-hand one.

Data Availability Statement

The MMS data (<https://cdaweb.gsfc.nasa.gov/>). The codes for the algorithm are available at the website: <http://doi.org/10.5281/zenodo.4678127>.

Acknowledgments

This work was supported by National Natural Science Foundation (NSFC) of China Grant (No. 41874190, 41922031, and 41774188). M. W. Dunlop is partly supported by Science & Technology Facilities Council (STFC) research grant ST/M001083/1, the NSFC grants 41574155 and 41431071, and the Natural Environment Research Council (NERC) grant NE/P016863/1. The authors are also thankful to the entire MMS team for providing the MMS data.

References

- Angelopoulos, V. (2008). The THEMIS mission. *Space Science Reviews*, 141(1–4), 5–34. <https://doi.org/10.1007/s11214-008-9336-1>
- Balogh, A., Carr, C. M., Acuña, M. H., Dunlop, M. W., Beek, T. J., Brown, P., et al. (2001). The Cluster magnetic field investigation: Overview of inflight performance and initial results. *Annales Geophysicae*, 19, 1207. <https://doi.org/10.5194/angeo-19-1207-2001>
- Berger, M. A. (1999). Introduction to magnetic helicity. *Plasma Physics and Controlled Fusion*, 41, B167. <https://doi.org/10.1088/0741-3335/41/12b/312>
- Burch, J. L., Moore, T. E., Torbert, R. B., & Giles, B. L. (2016). Magnetospheric Multiscale overview and science objectives. *Space Science Reviews*, 199(1–4), 5–21. <https://doi.org/10.1007/s11214-015-0164-9>
- Chanteur, G. (1998). Spatial interpolation for four spacecraft: Theory. In G. Paschmann, P. W. Daly (Eds.), *Analysis methods for multi-spacecraft data* (p. 349). Noordwijk, Netherlands: ESA Publ. Div.
- De Keyser, J., Dunlop, M. W., Darrouzet, F., & Décréau, P. M. E. (2007). Least-squares gradient calculation from multi-point observations of scalar and vector fields: Methodology and applications with cluster in the plasmasphere. *Annales Geophysicae*, 25, 971–987. <https://doi.org/10.5194/angeo-25-971-2007>
- Denton, R. E., Torbert, R. B., Hasegawa, H., Dors, I., Genestreti, K. J., Argall, M. R., et al. (2020). Polynomial reconstruction of the reconnection magnetic field observed by multiple spacecraft. *Journal of Geophysical Research: Space Physics*, 125, e2019JA027481. <https://doi.org/10.1029/2019ja027481>
- Dunlop, M. W., Haaland, S., Dong, X.-C., Middleton, H., Escoubet, P., Yang, Y.-Y., et al. (2018). Multi-point analysis of current structures and applications: Curlometer technique. In A. Keilling, O. Marghitu, & M. Wheatland (Eds.), *Electric currents in geospace and beyond*. Hoboken, NJ: John Wiley & Sons, Inc/AGU books. <https://doi.org/10.1002/9781119324522.ch4>
- Dunlop, M. W., Haaland, S., Escoubet, P., & Dong, X.-C. (2016). Commentary on accessing 3-D currents in space: Experiences from cluster. *Journal of Geophysical Research*, 121. <https://doi.org/10.1002/2016JA022668>
- Dunlop, M. W., Yang, Y.-Y., Yang, J.-Y., Luhr, H., Shen, C., Olsen, N., et al. (2015). Multi-spacecraft current estimates at swarm. *Journal of Geophysical Research*, 120. <https://doi.org/10.1002/2015JA021707>
- Dunlop, M. W. Y., Yang, Y.-Y., Yang, J.-Y., Lühr, H., & Cao, J.-B. (2020). Multi-spacecraft current estimates at swarm. In M. W. Dunlop, & H. Luehr (Eds.), *Multi-satellite data analysis. ISSI scientific reports*. Springer. https://doi.org/10.1007/978-3-030-26732-2_5
- Eastwood, J. P., Phan, T. D., Cassak, P. A., Gershman, D. J., Haggerty, C., Malakit, K., et al. (2016). Ion-scale secondary flux ropes generated by magnetopause reconnection as resolved by MMS. *Geophysical Research Letters*, 43, 4716–4724. <https://doi.org/10.1002/2016GL068747>
- Escoubet, C. P., Fehringer, M., & Goldstein, M. (2001). Introduction: The Cluster mission. *Annales Geophysicae*, 19, 1197–1200. <https://doi.org/10.5194/angeo-19-1197-2001>
- Fadanelli, S., Lavraud, B., Califano, F., Jacquey, C., Vernisse, Y., Kacem, I., et al. (2019). Four-spacecraft measurements of the shape and dimensionality of magnetic structures in the near-Earth plasma environment. *Journal of Geophysical Research: Space Physics*, 124. <https://doi.org/10.1029/2019JA026747>
- Friis-Christensen, E., Lühr, H., & Hulot, G. (2006). Swarm: A constellation to study the Earth's magnetic field. *Earth Planets and Space*, 58, 351–358. <https://doi.org/10.1186/bf03351933>

- Hamrin, M., Rönmark, K., Börlin, N., Vedin, J., & Vaivads, A. (2008). Gals: Gradient analysis by least squares. *Annales Geophysicae*, 26(11), 3491–3499. <https://doi.org/10.5194/angeo-26-3491-2008>
- Harris, E. G. (1962). On a plasma sheath separating regions of oppositely directed magnetic field. *Nuovo Cimento*, XXIII, 115. <https://doi.org/10.1007/bf02733547>
- Harvey, C. C. (1998). Spatial gradients and the volumetric tensor. In G. Paschmann, P. W. Daly (Eds.), *Analysis methods for multi-spacecraft data* (p. 307). The Netherlands: ESA Publications Division, Noordwijk.
- Kivelson, M. G., Khurana, K. K., alker, R. J. W., Kepko, L., & Xu, D. (1995). Flux ropes, interhemispheric conjugacy, and magnetospheric current closure. *Journal of Geophysical Research*, 10(A12), 27341–27350. <https://doi.org/10.1029/96JA02220>
- Lavraud, B., Zhang, Y. C., Vernisse, Y., Gershman, D. J., Dorelli, J., Cassak, P. A., et al. (2016). Currents and associated electron scattering and bouncing near the diffusion region at Earth's magnetopause. *Geophysical Research Letters*, 43, 6036–6043. <https://doi.org/10.1002/2016GL068359>
- Lee, L. C., Fu, Z. F., & Akasofu, S.-I. (1985). A simulation study of forced reconnection processes and magnetospheric storms and substorms. *Journal of Geophysical Research*, 90(A11), 896–910. <https://doi.org/10.1029/JA090iA11p10896>
- Liu, Y., Pu, Z. Y., Xie, L., Guo, R., Wang, X., Xiao, C., et al. (2018). Ion-scale structures in flux ropes observed by MMS at the magnetopause (in Chinese). *Chinese Journal of Space Science*, 38(2), 147–168. <https://doi.org/10.11728/cjss2018.02.147>
- Liu, Y. Y., Fu, H. S., Olshevsky, V., Pontin, D. I., Liu, C. M., Wang, Z., Chen, G., et al. (2019). SOTE: A nonlinear method for magnetic topology reconstruction in space plasmas. *The Astrophysical Journal Supplement Series*, 244, 31. <https://doi.org/10.3847/1538-4365/ab391a>
- Liu, Z.-X., Escoubet, C. P., Pu, Z., Laakso, H., Shi, J. Q., Shen, C., & Hapgood, M. (2005). The double star mission. *Annales Geophysicae*, 23, 2707–2712. <https://doi.org/10.5194/angeo-23-2707-2005>
- Liu, Z. X., & Hu, Y. D. (1988). Local magnetic reconnection caused by vortices in the flow field. *Geophysical Research Letters*, 12, 752. <https://doi.org/10.1029/gl015i008p00752>
- Lockwood, M., & Hapgood, M. A. (1998). On the cause of a magnetospheric flux transfer event. *Journal of Geophysical Research*, 103(A11), 26453–26478. <https://doi.org/10.1029/98JA02244>
- Lundquist, S. (1950). Magneto-hydrostatic fields. *Arkiv för Fysik*, 2, 361–365.
- McComas, C., Russell, T., Elphic, R. C., & Bame, S. J. (1986). The near-Earth cross-tail current sheet: Detailed ISEE 1 and 2 case studies. *Journal of Geophysical Research*, 91, 4287. <https://doi.org/10.1029/ja091ia04p04287>
- Ogilvie, K. W., Von Rosenvinge, T., & Durney, A. C. (1977). International Sun-Earth explorer: A three-spacecraft program. *Science*, 198, 131–138. <https://doi.org/10.1126/science.198.4313.131>
- Pollock, C., Moore, T. E., Jacques, A., Burch, J., Gliese, U., Saito, Y., et al. (2016). Fast plasma investigation for magnetospheric multiscale. *Space Science Reviews*, 199(1-4), 331–406. <https://doi.org/10.1007/s11214-016-0245-4>
- Pu, Z. Y., Zong, Q.-G., Fritz, T. A., Xiao, C. J., Huang, Z. Y., Fu, S. Y., et al. (2005). Multiple flux rope events at the high-latitude magnetopause: Cluster/rapid observation on 26 January, 2001. *Surveys in Geophysics*, 26(1-3), 193–214. <https://doi.org/10.1007/s10712-005-1878-0>
- Rong, Z. J., Wan, W. X., Shen, C., Li, X., Dunlop, M. W., Petrukovich, A. A., et al. (2011). Statistical survey on the magnetic structure in magnetotail current sheets. *Journal of Geophysical Research*, 116, A09218. <https://doi.org/10.1029/2011JA016489>
- Rong, Z. J., Wan, W. X., Shen, C., Li, X., Dunlop, M. W., Petrukovich, A. A., et al. (2012). Profile of strong magnetic field B_y component in magnetotail current sheets. *Journal of Geophysical Research*, 117, A06216. <https://doi.org/10.1029/2011JA017402>
- Russell, C. T., Anderson, B. J., Baumjohann, W., Bromund, K. R., Dearborn, D., Fischer, D., et al. (2016). The magnetospheric multiscale magnetometers. *Space Science Reviews*, 199(1-4). <https://doi.org/10.1007/s11214-014-0057-3>
- Russell, C. T., & Elphic, R. C. (1979). ISEE observations of flux transfer events at the dayside magnetopause. *Geophysical Research Letters*, 6(1), 33–36. <https://doi.org/10.1029/GL006i001p00033>
- Shen, C., Dunlop, M., Ma, Y. H., Chen, Z. Q., Yan, G. Q., Liu, Z. X., et al. (2011). The magnetic configuration of the high-latitude cusp and day-side magnetopause under strong magnetic shears. *Journal of Geophysical Research*, 116, A09228. <https://doi.org/10.1029/2011JA016501>
- Shen, C., Liu, Z., Li, X., Dunlop, M. W., Lucek, E. A., Rong, Z., et al. (2008a). Flattened Current sheet and its evolution in substorms. *Journal of Geophysical Research*, 113, A07S21. <https://doi.org/10.1029/2007JA012812>
- Shen, C., & Liu, Z. -X. (2005). Double star project master science operations plan. *Annales Geophysicae*, 23, 2851–2859. <https://doi.org/10.5194/angeo-23-2851-2005.Shen>
- Shen, C., Li, X., Dunlop, M., Liu, Z. X., Balogh, A., Baker, D. N., et al. (2003). Analyses on the geometrical structure of magnetic field in the current sheet based on cluster measurements. *Journal of Geophysical Research*, 108(A5), 1168. <https://doi.org/10.1029/2002JA009612>
- Shen, C., Li, X., Dunlop, M., Shi, Q. Q., Liu, Z. X., Lucek, E., & Chen, Z. Q. (2007). Magnetic field rotation analysis and the applications. *Journal of Geophysical Research*, 112, A06211. <https://doi.org/10.1029/2005JA011584>
- Shen, C., Rong, Z. J., & Dunlop, M. (2012b). Determining the full magnetic field gradient from two spacecraft measurements under special constraints. *Journal of Geophysical Research*, 117, A10217. <https://doi.org/10.1029/2012JA018063>
- Shen, C., Rong, Z. J., Dunlop, M. W., Ma, Y. H., Li, X., Zeng, G., et al. (2012a). Spatial gradients from irregular, multiple-point spacecraft configurations. *Journal of Geophysical Research*, 117, A11207. <https://doi.org/10.1029/2012JA018075>
- Shen, C., Rong, Z. J., Li, X., Liu, Z. X., Dunlop, M., Lucek, E., & Malova, H. V. (2008b). Magnetic configurations of tail tilted current sheets. *Annales Geophysicae*, 26, 3525–3543. <https://doi.org/10.5194/angeo-26-3525-2008>
- Shen, C., Yang, Y. Y., Rong, Z. J., Li, X., Dunlop, M., Carr, C. M., et al. (2014). Direct calculation of the ring current distribution and magnetic structure seen by Cluster during geomagnetic storms. *Journal of Geophysical Research: Space Physics*, 119. <https://doi.org/10.1002/2013JA019460>
- Shi, Q. Q., Shen, C., Dunlop, M. W., Pu, Z. Y., Zong, Q.-G., Liu, Z. X., et al. (2006). Motion of observed structures calculated from multi-point magnetic field measurements: Application to Cluster. *Geophysical Research Letters*, 33, L08109. <https://doi.org/10.1029/2005GL025073>
- Shi, Q. Q., Shen, C., Pu, Z. Y., Dunlop, M. W., Zong, Q. G., Zhang, H., et al. (2005). Dimensional analysis of observed structures using multipoint magnetic field measurements: Application to Cluster. *Geophysical Research Letters*, 32, L12105. <https://doi.org/10.1029/2005GL022454>
- Sibeck, D. G., Siscoe, G. L., Slavin, J. A., Smith, E. J., Bame, S. J., & Scarf, F. L. (1984). Magnetotail flux ropes. *Geophysical Research Letters*, 11(10), 1090–1093. <https://doi.org/10.1029/GL011i010p01090>
- Slavin, J. A., Baker, D. N., Craven, J. D., Elphic, R. C., Fairfield, D. H., Frank, L. A., Galvin, A. B., et al. (1989). CDAW 8 observations of plasmoid signatures in the geomagnetic tail: An assessment. *Journal of Geophysical Research*, 94(A11), 15153–15175. <https://doi.org/10.1029/JA094iA11p15153>
- Slavin, J. A., Lepping, R. P., Gjerloev, J., Goldstein, M. L., Fairfield, D. H., Acuna, M. H., et al. (2003). Cluster electric current density measurements within a magnetic flux rope in the plasma sheet. *Geophysical Research Letters*, 30(7), 1362. <https://doi.org/10.1029/2002GL016411>
- Slavin, J. A., Owen, C. J., & Kuznetsova, M. M. (1995). ISEE3 observations of plasmoids with flux rope magnetic topologies. *Geophysical Research Letters*, 22(15), 2061–2064. <https://doi.org/10.1029/95GL01977>

- Song, P., & Russell, C. T. (1999). Time series data analyses in space physics. *Space Science Reviews*, 87(3–4), 387–463. <https://doi.org/10.1023/a:1005035800454>
- Torbert, R. B., Dors, I., Argall, M. R., Genestreti, K. J., Burch, J. L., Farrugia, C. J., et al. (2020). A new method of 3-D magnetic field reconstruction. *Geophysical Research Letters*, 47, e2019GL085542. <https://doi.org/10.1029/2019GL085542>
- Torbert, R. B., Vaith, H., Granoff, M., Widholm, M., Gaidos, J. A., Briggs, B. H., et al. (2015). The electron drift instrument for MMS. *Space Science Reviews*, 199(1–4), 283–305. <https://doi.org/10.1007/s11214-015-0182-7>
- Vogt, J., Albert, A., & Marghitu, O. (2009). Analysis of three-spacecraft data using planar reciprocal vectors: Methodological framework and spatial gradient estimation. *Annales Geophysicae*, 27, 3249–3273. <https://doi.org/10.5194/angeo-27-3249-2009>
- Vogt, J., Paschmann, G., & Chanteur, G. (2008). Reciprocal vectors. In G. Paschmann, & P. W. Daly (Eds.), *Multi-spacecraft analysis methods revisited, ISSI sci. Rep., SR-008* (pp. 33–46). Dordrecht, Netherlands: Kluwer Academic Pub.
- Wang, J., Dunlop, M. W., Pu, Z. Y., Zhou, X. Z., Zhang, X. G., Wei, Y., et al. (2007). TC1 and Cluster observation of an FTE on 4 January 2005: A close conjunction. *Geophysical Research Letters*, 34, L03106. <https://doi.org/10.1029/2006GL028241>
- Xiao, C., Liu, W., Shen, C., Zhang, H., & Rong, Z. (2018). Study on the curvature and gradient of the magnetic field in Earth's cusp region based on the magnetic curvature analysis method. *Journal of Geophysical Research: Space Physics*, 123, 3794–3805. <https://doi.org/10.1029/2017JA025028>
- Zhang, C., Rong, Z. J., Shen, C., Klinger, L., Gao, J. W., Slavin, J. A., et al. (2020). Examining the magnetic geometry of magnetic flux ropes from the view of single-point analysis. *The Astrophysical Journal*, 903. <https://doi.org/10.3847/1538-4357/abba16>
- Zhang, Y. C., Liu, X. X., Shen, C., Fazakerley, A., Dunlop, M., Reme, H., et al. (2007). The magnetic structure of an earthward-moving flux rope observed by Cluster in the near-tail. *Annales Geophysicae*, 25, 1471–1476. <https://doi.org/10.5194/angeo-25-1471-2007>
- Zong, Q. G., Fritz, T., Fu, S., Pu, Z., Baker, D., Zhang, H., et al. (2004). Cluster observations of earthward flowing plasmoid in the tail. *Geophysical Research Letters*, 31, L18803. <https://doi.org/10.1029/2004GL020692>